Disturbed engram network caused by NPTXs downregulation underlies aging-related memory deficits

Tao Jin[1,2,3], Yang Yang[1,2,3], Yu Guo[1,3], Yi Zhang[1], Qiumin Le[1,2], Nan Huang[1,2], Xing Liu[1,2], Jintai Yu[1], Lan Ma[1,2] and Feifei Wang[1,2]*

[1] State Key Laboratory of Medical Neurobiology and MOE Frontiers Center for Brain Science, Institutes of Brain Science, School of Basic Medical Sciences, Department of Neurology and National Center for Neurological Disorders, Huashan Hospital, Fudan University, Shanghai 200032, China.

[2] Research Unit of Addiction Memory, Chinese Academy of Medical Sciences (2021RU009), Shanghai 200032, China.

[3] These authors contributed equally: Tao Jin, Yang Yang, Yu Guo

*Corresponding author. Email: ffwang@fudan.edu.cn

Abstract

Engram cells storing specific memories are allocated to separate neuronal ensembles, which preferentially recruit either excitatory or inhibitory inputs to drive precise memory expression. However, how these formed neuronal ensembles maintain their stability, and whether the disturbed stability contributes to aging-related memory deficits remain elusive. Here, we show that neuronal pentraxin1 (NPTX1) facilitates Kv7.2-mediated inhibition of *Fos*$^+$ ensemble hyperexcitability, thereby restricting its response to excitatory inputs from medial entorhinal cortex (MEC) and promoting memory expression in the fear context. Meanwhile, NPTX2 facilitates the perisomatic inhibition of the *Npas4*$^+$ ensemble by parvalbumin$^+$ (PV$^+$) interneurons, thus preventing fear memory overgeneralization. Pharmacological activation of Kv7.2 or chemogenetic activation of PV$^+$ interneurons repaired memory deficits caused by engram specific NPTXs depletion. Contextual fear memory precision and NPTXs expression in dentate gyrus (DG) engram cells are decreased in aged mice. Overexpression of NPTX1 in *Fos*$^+$ ensemble or AMPAR binding domain of NPTX2 in *Npas4*$^+$ ensemble rescued memory imprecision. These findings elucidate that the coordination of NPTXs prevents engram ensembles from becoming hyperactive and provide a causal link between engram network destabilization and aging-associated memory deficits.

Key Words: Engram stability, NPTXs, aging, memory deficits

Introduction

Memories are believed to be encoded in sparse neuronal ensembles (engram cells) that are activated by specific learning experiences[1,2]. Neurons recruited to engrams are more stably connected than those that are not[3]. Memory accessibility and precision are shaped by the plasticity of engram network, and require the long-lasting stabilization of the recruited engram network. However, the molecular mechanisms underlying the maintenance of the dormant, but stable engram network remain unknown. In addition, memory precision progressively declines with age, and is considered as one of the predominant hallmarks of aging-associated cognitive dysfunctions[4,5], while it remains to be elucidated how the disturbed engram network leads to aging-related memory deficits.

Cell-adhesion molecules (CAMs) are a super family which play an irreplaceable role in synaptic plasticity through mediating the bidirectional organization of synaptic compartments[6]. NPTXs are a subfamily of CAMs primarily expressed in excitatory neurons. NPTXs consist of NPTX1, NPTX2 and their receptor NPTXR[7]. Pre-synaptic secreted NPTX1 and NPTX2 form disulfide-linked heteromultimers with post-synaptic NPTXR to promote the clustering of α-amino-3-hydroxy-5-methyl-4-isoxazolepropionic acid (AMPA) type glutamate receptors (AMPARs)[8,9]. Further studies identify NPTX1 functions as a pro-apoptotic protein[10] that restricts excitatory synaptic transmission[11]. In contrast, NPTX2 maintains excitatory homeostasis by adaptively enhancing circuit inhibition[12,13]. These findings raise the possibility that NPTX1 and NPTX2 function as the potential molecular substrates for stabilizing the

excitatory and inhibitory inputs onto distinct neuronal ensembles. NPTXs are also considered as prognostic biomarkers for neurodegeneration whose expressions are decreased in Alzheimer's disease (AD), schizophrenia or even mild cognitive impairment (MCI) patients[14-16]. However, the causal link between NPTXs reduction-induced engram network destabilization and aging-related memory deficits remain unclear.

The tracing of neuronal circuits involved in specific memory formation is enabled by measuring the expression of selectively activated immediate early genes (IEGs). The DG engram cells within the equivalent memory contain functionally divergent *Fos*$^+$ and *Npas4*$^+$ neuronal ensembles, which drive precise memory expression by recruiting excitatory and inhibitory (E/I) circuits[17]. The expression of NPTX1 and NPTX2 are both abundant in DG[18]. In this study, we found that the maintenance of engram network stability requires NPTX1 and NPTX2 to coordinately stabilize the excitatory inputs to the *Fos*$^+$ ensemble and the inhibitory inputs to the *Npas4*$^+$ ensemble. Engram network hyperactivity, caused by NPTXs downregulation in DG engram ensembles contributed to aging-related contextual fear memory imprecision, including impaired memory expression in the fear context and overgeneralization in the non-fear context, which was rescued by restoring NPTXs expression in different engram ensembles. Our findings elucidate the critical role of NPTXs in stabilizing the formed engram network by controlling DG excitatory and inhibitory inputs, and establish a causal link between engram network destabilization and aging-associated memory deficits.

Results

NPTX1 restricts MEC excitatory inputs onto DG *F*-RAM ensemble

Fos and *Npas4*-dependent robust activity marking (*F*-RAM and *N*-RAM) reporter systems were used to label engram ensembles with mKate2 reporter by off Dox[17]. *Npas4-CreER*^{T2} mice in which the endogenous *Npas4* promoter drives the expression of *CreER*^{T2} were generated to label *Npas4*$^{+}$ ensembles with EGFP reporter by 4-hydroxytamoxifen (4-OHT) intraperitoneal (i.p.) injection (Figure. S1A-1D). A combination of these two activity-dependent labelling strategies (Figure. S1E) was used simultaneously to label engrams activated by contextual fear conditioning (CFC, 0.5 mA, 1 s, 3 trials). The EGFP^{+} neurons showed substantial overlap with mKate2^{+} *N*-RAM ensemble while showed minimal colocalization with mKate2^{+} *F*-RAM ensemble (Figure. S1F-1G). These results confirm that *Fos*$^{+}$ and *Npas4*$^{+}$ engram cells in DG labeled by *F*-RAM and *N*-RAM reporters are distinct populations.

The upstream inputs of *F*- and *N*-RAM neuronal ensembles from medial septum (MS), horizontal limb of the diagonal band (HDB), perirhinal cortex (PRh), lateral entorhinal cortex (LEC), medial entorhinal cortex (MEC) and DG were detected by rabies virus (RV) tracing (Figure 1A-1B). *F*-RAM ensemble formed more connections with MS and MEC, while *N*-RAM ensemble received more inputs from DG local neurons (Figure 1C). The majority of dsRed^{+} neurons in MS were co-labelled with the cholinergic neuron marker choline acetyltransferase (ChAT, Figure 1D-1E), and DG *F*-RAM neurons received more excitatory inputs from MEC than *N*-RAM neurons (Figure 1F-1G).

98 NPTXs were found to be predominantly involved in E/I synaptic homeostasis rather
99 than cholinergic signaling[9,19]. To test whether NPTXs modulate the stability of the
100 synaptic transmission between MEC and DG *Fos*$^{+}$ ensemble, *Nptx1*$^{fl/fl}$, *Nptx2* $^{fl/fl}$
101 conditional knockout (*Nptx1* cKO, *Nptx2* cKO) mice were generated (Figure S2A-2B).
102 Ribosome-associated transcripts of *F*-RAM and *N*-RAM ensembles were enriched
103 from *Nptxs* cKO mice and their WT littermates (Figure S2C-2D), and qPCR against
104 *Nptx1* exon 3 and *Nptx2* exon 2 was performed to confirm the knockout efficiency in
105 *F*- or *N*-RAM ensembles. *Nptx2* expression was unaffected when *Nptx1* was depleted
106 and vice versa (Figure S2E-2L). Immunostaining of NPTX1 and NPTX2 further
107 confirmed the knockout efficiency in DG engram ensembles (Figure S3).
108 *AAV-CaMKIIα-ChR2-mCherry* was then injected into MEC of *Nptx1* cKO, *Nptx2* cKO
109 mice and their WT littermates, and the virus mixture of *AAV-F-RAM-Cre* with Cre
110 recombinase-dependent *AAV-DIO-H2B-EGFP* was injected into DG to knock out *Nptxs*
111 in *Fos*$^{+}$ ensemble. Opto-evoked excitatory post-synaptic currents (oEPSCs) from MEC
112 were recorded on EGFP^{-} (*F*-RAM^{-}) and EGFP^{+} (*F*-RAM^{+}) cells (Figure 1H). The
113 amplitude of oEPSCs on EGFP^{+} cells was larger in the *Nptx1* cKO group (Figure 1I-
114 1J), whereas this effect was not found in the *Nptx2* cKO mice (Figure 1K-1L). These
115 data indicate that NPTX1 plays an important role in dampening the excitatory synaptic
116 transmission between MEC and DG *Fos*$^{+}$ ensemble.
117

118 **NPTX1 facilitates I_M current and membrane expression of Kv7.2 in DG *F*-RAM**
119 **ensemble**

Action potential (AP) recordings were performed to examine whether neuronal excitability of the engram ensembles was changed after *Nptxs* knockout (Figure 2A-2C). *F*-RAM engram cells lacking *Nptx1,* but not *Nptx2,* exhibited upward shift of the neuronal spiking curve after step-increment current injections, lower resting membrane potential (RMP) and rheobase (Figure 2D-2K), indicating increased excitability of *F*-RAM engram cells after *Nptx1* knockout. KCNQ2 (Kv7.2) pairs with the KCNQ3 (Kv7.3) subunit to form KCNQ2/3 heterotetramers, which are the primary molecular substrate of M-current (I_M) involved in regulating neuronal excitability[20,21]. Application of the KCNQ2/3-selective blocker XE991 resulted in a reduction of I_M amplitude on DG *F*-RAM engram cells (Figure 2L-2M). *Nptx1* depletion exerted the similar inhibitory effect of XE991 on I_M amplitude (Figure 2N-2O). Co-immunoprecipitation (Co-IP) of the DG lysate confirmed the interaction between NPTX1 and Kv7.2 (Figure 2P). Immunostaining analysis further revealed that *Nptx1* ablation decreased Kv7.2 membrane expression in *F*-RAM engram cells (Figure 2Q-2R), which was not observed in *Nptx2* cKO group (Figure 2S-2T). Taken together, these results indicate that NPTX1 restrains the excitatory synaptic transmission between MEC and DG Fos^+ ensemble by facilitating Kv7.2 membrane expression-mediated inhibition of neuronal hyperexcitability.

NPTX2 in *N*-RAM ensemble facilitates the perisomatic inhibition by PV^+ interneurons in DG

Rabies tracing confirmed *N*-RAM ensemble received more inputs from DG local

142 neurons (Figure 1C), leading us to wonder whether NPTX2 was specifically involved
143 in *Npas4*$^{+}$ engram-DG local neuron synaptic connection. Immunostaining showed that
144 parvalbumin^{+} (PV^{+}) and somatostatin^{+} (SST^{+}) interneurons, two major subtypes of
145 GABAergic interneurons in DG[22] that separately target perisomatic compartments and
146 distal apical dendrites of granule cells[23] were both recruited by DG *Fos*$^{+}$ and *Npas4*$^{+}$
147 engram cells after CFC. However, *Npas4*$^{+}$ engram cells received more PV^{+} but not
148 SST^{+} inputs in DG (Figure 3A-3B, Figure S4A-4B).
149 To test the involvement of NPTX2 in the synaptic transmission between *N*-RAM
150 ensemble and DG interneurons, the viral mixture of *AAV-N-RAM-Cre, AAV-DIO-ChR2-*
151 *EYFP, AAV-PV/SST-Flp* and Flp recombinase-dependent *AAV-fDIO-mCherry* was
152 injected into DG of *Nptx1* cKO, *Nptx2* cKO mice and WT littermates. The specificity
153 of *AAV-SST-Flp* and *AAV-PV-Flp* was confirmed by immunostaining with anti-SST and
154 anti-PV antibodies (Figure S4C-4D, Figure S5A). Opto-evoked paired-pulse ratio (PPR)
155 and AMPAR/N-methyl-D-aspartate receptor (NMDAR) (A/N) ratio were recorded on
156 SST^{+} or PV^{+} interneurons according to mCherry expression, morphology and location
157 (Figure 3C-3D, Figure S4E-4F). *Nptxs* depletion in *N*-RAM ensemble reduced pre-
158 synaptic glutamate release (Figure S4G-4H, S4K-4L, Figure S5B-5E,), consistent with
159 previous studies that NPTXs family promotes pre-synaptic glutamate release[19,24]. *Nptx2*
160 knockout in *N*-RAM ensemble exerted no effect on A/N ratio of SST^{+} interneurons
161 (Figure S4I-4J, S4M-4N), whereas *Nptx2,* but not *Nptx1* depletion in *N*-RAM ensemble
162 significantly decreased AMPAR-mediated EPSC and A/N ratio on PV^{+} interneurons
163 (Figure 3E-3J). Previous studies found that NPTX2 binds AMPAR subunit GluA4 on

164 PV^+ interneurons to regulate network excitatory/inhibitory balance[12,25].
165 Immunostaining confirmed that *Nptx2* depletion in *N*-RAM ensemble decreased the
166 expression of GluA4 on PV^+ interneurons (Figure 3K-3L).
167 To examine whether NPTX2-dependent plasticity applies to GABAergic CCK^+ cells,
168 the viral mixture of *AAV-N-RAM-Cre, AAV-DIO-ChR2-EYFP* with *AAV-vGAT2-Flp-*
169 dependent expression of *AAV-CCK-fDIO-mCherry* was injected into DG of WT and
170 *Nptx2* cKO mice to label the GABAergic CCK^+ cells (Figure S6A-6C). Opto-evoked
171 PPR and A/N ratio were recorded on $mCherry^+$ interneurons, and no differences were
172 detected after *Nptx2* depletion in *N*-RAM ensemble (Figure S6D-6G). These data
173 suggest that NPTX2-dependent interneuron plasticity was specific to PV^+ interneurons.
174 The disturbed PV^+ interneuron plasticity caused by *Nptx2* depletion led us to speculate
175 whether the inhibitory inputs received by *N*-RAM ensemble was also affected. A viral
176 mixture of *AAV-fDIO-ChR2-mCherry*, *AAV-N-RAM-Cre* and *AAV-Flex-EGFP-Nptx2*
177 *shRNA (Nptx2 sh)* was injected into DG of *PV-Flpe* mice, and opto-evoked inhibitory
178 post-synaptic currents (oIPSCs) and PPR were recorded on *N*-RAM cells (Figure 3M-
179 3N). The increased PPR in the *Nptx2 shRNA* group indicates the reduction of pre-
180 synaptic γ-aminobutyric acid (GABA) release from PV^+ interneurons (Figure 3O-3P),
181 leading to the reduced inhibition $Npas4^+$ engram cell received (Figure 3Q-3R). Taken
182 together, these data indicate that NPTX2 facilitates the inhibitory synaptic transmission
183 between DG $Npas4^+$ engram cells and PV^+ interneurons by the AMPAR-dependent
184 mechanism.
185

186 **NPTX1 in DG *F*os$^+$ ensemble and NPTX2 in DG *Npas4*$^+$ ensemble facilitate the**
187 **precise expression of contextual fear memory**

188 To investigate the involvement of NPTXs-dependent maintenance of engram network
189 stability on behavioral outputs, the viral mixture of *AAV-F-RAM-Cre* or *AAV-N-RAM-*
190 *Cre* combined with *AAV-DIO-EYFP* was injected into DG of young *Nptx1* cKO, *Nptx2*
191 cKO mice and their respective WT littermates. Mice were tested on day 3 in context A
192 and context C after fear conditioning (Figure 4A-4C, 4H-4J). The freezing level during
193 conditioning was not different between *Nptx1* cKO, *Nptx2* cKO mice and their WT
194 littermates (Figure S7A-7D). Interestingly, *Nptx1* depletion in *F*-RAM ensemble
195 decreased freezing in context A (Figure 4D-4E), whereas *Nptx2* depletion in *F*-RAM
196 neuronal ensemble caused no differences in freezing level in both contexts (Figure 4F-
197 4G). *Nptx1* knockout in DG *N*-RAM ensemble did not affect the freezing level in either
198 context (Figure 4K-4L), whereas *Nptx2* knock out in DG *N*-RAM ensemble increased
199 the freezing level in the non-fear context C on day 3, indicating overgeneralization of
200 contextual fear memory (Figure 4M-4N).

201 In addition, when mice were exposed to a novel context (context N) quite different with
202 context A or context C, *Nptx1* or *Nptx2* was knocked out in randomly labeled *F*- or *N*-
203 RAM neurons (Figure 4O-4Q), and no differences in freezing were found between
204 *Nptxs* cKO and WT controls (Figure S7E-7F, Figure 4R-4U), indicating the fear
205 context-specific effect of *Nptxs*. Moreover, *Nptxs* depletion in both ensembles had no
206 effect on mice's locomotion, anxiety or depression levels (Figure S8-S10).

207 Taken together, these data suggest that the precise expression of contextual fear memory,

208 including high freezing level in the fear context but low freezing level in the non-fear
209 context requires the coordination of NPTX1 and NPTX2 functioning in distinct
210 ensembles.
211

212 **Pharmacological activation of Kv7.2 or chemogenetic activation of PV$^+$**
213 **interneurons ameliorates memory deficits induced by NPTXs depletion in DG**
214 **engrams**

215 The Kv7.2 activator retigabine, a clinically used anticonvulsant[26], was i.p. injected 30
216 min before mice were tested in the fear context A and non-fear context C (Figure 5A-
217 5C). Retigabine had no effect on the freezing level of WT mice in either context,
218 whereas it restored the reduced freezing level in context A when NPTX1 was depleted
219 in *F*-RAM ensemble but not in *N*-RAM ensemble (Figure 5D-5G, Figure S11A-11B).
220 To rescue memory overgeneralization induced by *Nptx2* knockout in *N*-RAM ensemble,
221 the designer receptors exclusively activated by designer drugs (DREADDs) were used
222 to activate PV$^+$ interneurons. The viral mixture of *AAV-N-RAM-Cre*, *AAV-Flex-EGFP-*
223 *Nptx2 shRNA* and *AAV-fDIO-hM3Dq-mCherry* was injected into the DG of *PV-Flpe*
224 mice and clozapine N-oxide (CNO) was administrated by i.p. injection 30 min before
225 the mice were tested in context A and context C (Figure 5H-5J). Chemogenetic
226 activation of local DG PV$^+$ interneurons had no effect on the freezing level of control
227 group infected with *Scramble shRNA*, while it reduced the freezing level of mice in
228 context C when *Nptx2* was knocked down in *N*-RAM ensemble instead of *F*-RAM
229 ensemble (Figure 5K-5N, Figure S11C-11D).

230

231 **Downregulation of *Nptxs* in DG engrams in aged mice**

232 Maladaptive changes in the expression of functional synaptic protein leading to
233 neuronal network destabilization and cognitive impairment, are central hallmarks
234 associated with physiological brain aging[27]. NPTXs are considered as biomarkers of
235 synaptic dysfunction and cognitive impairment[7,16]. To investigate whether *Nptxs*
236 expression in DG changes during physiological aging, young (3m) and aged (18m) mice
237 were sacrificed 15 min, 30 min, 60 min and 120 min after CFC or under homecage (HC)
238 condition, smFISH was used to assess their mRNA expression (Figure 6A-6D, S12A-
239 12D).

240 *Fos*$^+$ and *Npas4*$^+$ cell numbers after CFC were decreased in the DG of aged mice,
241 especially at 30 and 60 min, indicating decreased activation of neurons during learning
242 in aged mice (Fig S12E-12F). *Nptx1* was expressed in all DG granule cells, although
243 the overall *Nptx1*$^+$ fluorescence intensity was not significantly decreased in aged mice
244 (Figure 6E), the specific expression of *Nptx1* in *Fos*$^+$ and *Npas4*$^+$ engram cells were
245 reduced (Figure 6F, Figure S12G). NPTX2 was also seen as a neuronal IEG protein[14],
246 both *Nptx2*$^+$ cell numbers and the average fluorescence intensity of *Nptx2 mRNA* in
247 *Fos*$^+$ and *Npas4*$^+$ engram cells were decreased in aged mice (Figure 6G-6H, Figure
248 S12H). These findings indicate the downregulation of *Nptx1* and *Nptx2* in *Fos*$^+$ and
249 *Npas4*$^+$ engram cells in aged mice.

250 The expression of contextual fear memory in young and aged mice were further
251 assessed. When exposed to strong fear conditioning (0.5 mA, 1 s, 3 trials), aged mice

252 froze more in the non-fear context C, suggesting memory overgeneralization (Figure 6I,
253 6K-6L). However, when exposed to mild fear conditioning (0.3 mA, 1 s, 1 trial), aged
254 mice froze less in the fear context A (Figure 6J, 6M-6N), suggesting memory retrieval
255 impairment. These results demonstrate that aging impairs the precise expression of
256 contextual fear memory.
257

258 **NPTXs overexpression in DG engrams rescued memory deficits in aged mice**

259 Consistent with the decreased number of *Fos*$^+$ and *Npas4*$^+$ cells in DG after CFC, the
260 number of cells labelled by the *F*- and *N*-RAM systems were both reduced in DG of
261 aged mice (Figure S12I-12J). Ribosome-associated transcripts of *F*-RAM and *N*-RAM
262 ensembles activated in the home cage or by CFC were analyzed (Figure S13A). Gene
263 ontology (GO) analysis revealed clusters of differentially expressed genes (DEGs)
264 related to synaptic plasticity and cell communication between *F*-RAM and *N*-RAM
265 ensembles, which were more significant after CFC (Figure S13B). In addition, a
266 minority of DEGs overlapped between *F*- and *N*-RAM ensembles during aging (Figure
267 S13C-13D). DEGs in *F*-RAM during aging were preferentially enriched in pathways
268 regulating neuronal excitability, including membrane potential and potassium ion
269 import, whereas DEGs in *N*-RAM during aging were preferentially enriched in
270 AMPAR-mediated glutamatergic transmission and others (Figure S13E), suggesting
271 different pathways involved in engram network plasticity during aging between *F*- and
272 *N*-RAM ensembles.

273 Decreased Kv7.2 membranes expression on c-Fos$^+$ engram cells (Figure 7A-7B) and

274 NPTX1-Kv7.2 interaction in DG (Figure 7C-7D, S14A) were observed in aged mice.
275 AAV-DIO-Nptx1-EYFP was constructed to overexpress NPTX1 in a Cre-dependent
276 way (Figure S14B). Aged mice were subjected to the mild fear conditioning protocol
277 (0.3 mA, 1 s, one shock). Overexpression of NPTX1 in *F*-RAM ensemble, but not in
278 *N*-RAM ensemble increased the freezing level of aged mice in the fear context A
279 (Figure 7E-7K, Figure S14C-14D). Decreased GluA4 expression on PV^+ interneurons
280 and PV^+ fluorescence intensity surrounding $Npas4^+$ engram cells were observed in aged
281 mice (Figure 7L-7O), which are consistent with the phenotype of *Nptx2* depletion in
282 young mice (Figure 3). Aged mice overexpressing the AMPAR binding domain of
283 NPTX2 (NPTX2-PTX)[18] in *N*-RAM ensemble, but not in *F*-RAM ensemble rescued
284 overgeneralization in context C during retrieval (Figure 7P-7V, Figure S14E-14F).
285 However, overexpression of NPTX1 and NPTX2-PTX in young mice had no effect on
286 freezing levels when tested in either context A or context C (Figure S15). These data
287 confirm that DG engram network hyperactivity caused by NPTXs downregulation
288 underlies aging-associated memory imprecision, and that re-stabilization of NPTX1-
289 dependent MEC-Fos^+ engram excitatory circuit and NPTX2-dependent DG PV^+
290 interneuron-$Npas4^+$ engram inhibitory circuit is able to repair memory deficits in aged
291 mice.
292

293 **Discussion**

294 Contextual learning activates distinct Fos^+ and $Npas4^+$ engram ensembles, recruiting
295 enhanced excitatory and inhibitory circuits respectively to modulate memory-guided

296 adaptive behaviors. However, fundamental questions still remain: how the recruited
297 engram network maintains its stability and whether aging-related memory imprecision
298 associates with engram network destabilization. Our study identified NPTXs as the
299 molecular substrates that prevent network hyperactivity and maintain memory
300 precision. Although the NPTXs expression are not specific to *Fos*$^+$ and *Npas4*$^+$ engram
301 cells, the functional specificity of NPTXs should be placed into specific engram circuits
302 to be manifested, and the maintenance of circuit stability depends on the stable
303 expression of NPTX1 and NPTX2 specifically. Molecules and circuits, they are
304 interdependent, both are essential for ensuring precise behavioral outputs.
305 NPTX1 plays a critical role in stabilizing the excitatory synaptic connection between
306 MEC and DG *Fos*$^+$ engram cells via facilitating Kv7.2 membrane expression-
307 dependent inhibition of neuronal hyperexcitability to promote memory retrieval. Our
308 data demonstrate that NPTX1 interacts with a specific potassium channel Kv7.2 *in vivo*,
309 although it might not be a direct interaction and probably requires other auxiliary
310 proteins such as syntaxin[28], we provide a possible explanation for NPTX1 to regulate
311 neuronal excitability beyond its classical role in glutamate signaling. Our behavioral
312 output caused by *Nptx1* depletion in *F*-RAM ensemble was inconsistent with the results
313 of Sun *et al*[17] that chemogenetic activation of *F*-RAM ensemble or optogenetic
314 inhibition of MEC-DG circuit promoted or inhibited memory generalization. That's
315 probably because chemogenetic or optogenetic manipulation was transient, while *Nptx1*
316 depletion somehow mimics the persistent activation, leading to engram
317 hyperexcitability and decreased the signal-to-noise ratio (SNR) of MEC-*Fos*$^+$ ensemble

excitatory transmission during memory retrieval. Besides, a number of studies support the view that MEC inputs onto DG regulate memory retrieval[29,30].

NPTX2 stabilizes the inhibitory synaptic connection between DG local PV^+ interneurons and *N*-RAM ensemble to suppress memory overgeneralization, consistent with Sun *et al*'s report that *N*-RAM ensemble contributed to memory discrimination[17]. Their finding confirmed the involvement of CCK^+ interneurons, while our finding illustrated the importance of NPTX2 in mediating PV^+ interneurons plasticity. We speculate that *N*-RAM ensemble-dependent mediation of memory discrimination may require the coordination of both CCK^+ and PV^+ GABAergic interneurons as they have been found to exert complementary roles in recruiting perisomatic inhibition[31,32] while NPTX2 specifically regulates the functional connection between PV^+ interneurons and *Npas4*$^+$ engram cells. NPTX2 was found as a downstream protein of NPAS4[33,34], which explained the coincidence of the weakened perisomatic inhibition caused by *Nptx2* knockout with the finding of *Npas4* depletion by Elizabeth A *et al*'s [35]. As a neuronal IEG, Npas4 upregulates perisomatic inhibitory synapses when activated,[34,36] to scale down the level of network activity in response to neuronal excitation, but the specific mechanism remains to be elucidated. Our study provide the downstream molecular mechanism for Npas4 activation-dependent mediation of memory precision. The specificity of NPTX2 functions in *Npas4*$^+$ ensemble but not in *Fos*$^+$ ensemble to regulate memory discrimination can also be supported by the study by Ee-Lynn *et al* that knockdown of *Nptx2* in *Fos*$^+$ ensemble had no effect on the perisomatic inhibition received from PV^+ interneurons[37].

340 Memory precision changes dynamically across the lifespan, young individuals only
341 form gist-like memories and slowly develop into precise episodic memories as the brain
342 matures, then the ability to retrieve specific information declines with age.
343 Understanding the maladaptive changes in the engram network stability during aging
344 may provide insights to combat aging-induced cognitive deficits. NPTXs are classic
345 synaptic proteins that may also be prognostic biomarkers in cognitive and mental
346 disorders, such as AD and schizophrenia[14,15]. *Nptx2* was also seen as a neuronal IEG.
347 Our smFISH results showed that the total number of *Nptx2*$^{+}$ cells and the expression of
348 *Nptx2* in engram cells were both downregulated in DG during aging, whereas the
349 overall downregulation of *Nptx1* was not observed in aged mice, indicating that NPTX2
350 was more sensitive to aging. That is to say, along with aging, *Nptx2* downregulation-
351 induced disruption of local perisomatic inhibition of DG engram occurs before *Nptx1*
352 downregulation-induced disruption of MEC-DG engram excitatory long-range
353 projection, which probably explains why generalization always occurs before amnesia
354 in aged individuals. The findings of Ramsaran *et al* showed that extracellular
355 perineuronal nets-dependent functional maturation of PV^{+} interneurons promotes
356 sparse engram formation and memory precision during brain development[38]. Our study
357 elucidated that engram network hyperactivity, caused by NPTXs downregulation
358 contributes to aging-related memory imprecision and provided potential synaptic and
359 molecular strategies to mitigate different phenotypes of aging-related memory
360 imprecision, such as amnesia and overgeneralization respectively.

361 **Data availability**

The *F*- and *N*-RAM engram cells RNA-seq data have been submitted to NCBI Gene Expression Omnibus (GEO) under accession number PRJNA1067898.

Code availability

Custom codes will be provided upon request.

Acknowledgement

This work was supported by grants from the STI2030-Major Projects (2021ZD0203500 to FFW and LM, 2021ZD0202100 to XL), the Natural Science Foundation of China (32222033 to FFW, 31930046 and 82021002 to LM, 32171041 to XL, 31970543 and 32270660 to QML), the CAMS Innovation Fund for Medical Sciences (2021-I2M-5-009 to LM and XL). We thank Prof. Yingxi Lin (The University of Texas Southwestern Medical Center, Texas, USA) for providing the *AAV-Fos-RAM-d2tTA-TRE-mKate2* and *AAV-Npas4-RAM-d2tTA-TRE-mKate2* plasmids.

Author contributions

F.W., L.M. and T.J. designed the research. T.J. and Y.Y. conducted the AAV vector construction, virus injection, immunostaining, Co-IP, smFISH, Ribo Tag purification and the behavioral experiments. T.J. carried out the electrophysiology recordings. N.H., Y.G., Y.Z and Q.L. contributed to the bioinformatics analysis. T.J., Y.Y. J.Y, and X.L. analyzed the data and T.J. carried out the statistical analysis and drafted the manuscript. L.M. and F.W. supervised the project and revised the paper.

Competing interests

The authors declare no competing financial interests.

Methods

384 **Animals**

385 All animals used in this study were listed as follows: adult C57BL/6J male mice (3 m)
386 from the SLAC Laboratory Animal Company (Shanghai, China), aged C57BL/6J male
387 mice (16-18 m) from the Aniphe Biolaboratory Inc. (Nanjing, China) and *PV-Flpe*
388 (021191) mice from the Jackson Laboratory (CA, USA). CRISPR-Cas9 mediated
389 construction of *Nptx1*$^{fl/fl}$, *Nptx2*$^{fl/fl}$ conditional knockout (*Nptx1* cKO, *Nptx2* cKO) mice
390 targeting exon 3 and exon 2 respectively were generated by the Biocytogen Co. (Beijing,
391 China) and *Npas4-CreER*^{T2} mice were generated by Shanghai Model Organisms center,
392 Inc (Shanghai, China). *Npas4-CreER*^{T2} and *PV-Flpe* mice were bred to C57BL/6J mice
393 for more than six generations, *Nptx1*$^{fl/fl}$, *Nptx2*$^{fl/fl}$ mice and their respective wild-type
394 (WT) littermates were obtained from self-crossing of *Nptx1*$^{fl/+}$, *Nptx2*$^{fl/+}$ (heterozygous)
395 mice. Genotypes were determined by polymerase chain reaction (PCR) of mouse toe
396 DNA samples. The primers for genotyping PCR were as follows: 5' -
397 GCTGTAGGGATGCTTGTCTCTGGTG - 3' and 5' -
398 AGAAAAGCTGACCCAAGGTCTCTGC - 3' for *Nptx1* 5' *loxP,* 5' -
399 ATTAGCTGCCAGATCTTAGCCCCCT - 3' and 5' -
400 GTGTGTGTCCCTGGTGGTGAAGTTT - 3' for *Nptx1* 3' *loxP,* 5' -
401 GAATGGCTCGAGGCAGGTCCAGTTT - 3' and 5' -
402 CGTTACTAAACCCCAGACAGCTCCG - 3' for *Nptx2* 5' *loxP,* 5' -
403 AGTTCTGCCTCTGTTCATCTTGCCA - 3' and 5' -
404 TTCACCTGACCCTTCTGTTCACGAC - 3' for *Nptx2* 3' *loxP,* 5' -
405 AGAGCCTGAGCGAAAAGACC - 3', 5' - CTGCTCACCTCCAGCAAAGA - 3' and

406 5' - CGCGCGCCTGAAGATATAGA - 3' for *Npas4-CreER*^{T2}. Male offsprings at 8-12
407 weeks of age were used in following experiments, which were randomly assigned to
408 groups. All mice were housed on a 12 hr light/dark cycle (light on from 8 a.m. to 8 p.m.)
409 with access to food and water *ad libitum*. All experiment procedures were strictly in
410 accordance with the National Institutes of Health Guide for the Care and Use of
411 Laboratory Animals, and were approved by Animal Care and Use Committee of the
412 animal facility at Fudan University.

413 **Viral vectors**

414 *AAV-Fos-RAM-d2tTA-TRE-mKate2* and *AAV-Npas4-RAM-d2tTA-TRE-mKate2*
415 plasmids were kind gifts from Prof. Yingxi Lin (The University of Texas Southwestern
416 Medical Center, Texas, USA). To generate *AAV-Fos-RAM-d2tTA-TRE-Cre* and *AAV-*
417 *Npas4-RAM-d2tTA-TRE-Cre* plasmids, *mKate2* in *AAV-Fos-RAM-d2tTA-TRE-mKate2*
418 and *AAV-Npas4-RAM-d2tTA-TRE-mKate2* plasmids was replaced with the *Cre*
419 sequence obtained by PCR from *pAAV-Cre-GFP* (Addgene: 68544). *pAAV-CMV-*
420 *bGlobin-Flex-EGFP-MIR30-Scramble-shRNA*, *pAAV-CMV-bGlobin-Flex-EGFP-*
421 *MIR30-Nptx2-shRNA* and *pAAV-CMV-DIO-Nptx2-PTX-P2A-EGFP* were used in our
422 previous paper[18]. To generate *pAAV-Ef1α-DIO-Nptx1-T2A-EYFP*, the coding sequence
423 for mouse *Nptx1* with *T2A* was generated by Azenta US, Inc. (Suzhou, China) and was
424 subcloned into *pAAV-Ef1α-DIO-EYFP* (Addgene: 27056). Adeno-associated viruses
425 (AAVs) described above were packaged by OBiO Technology Co., Ltd (Shanghai,
426 China) into serotype 9. *AAV*$_9$*-Ef1α-Flex-NBL10* (69971) and *AAV*$_9$*-Ef1α-DIO-ChR2-*
427 *EYFP* (S0199-9-H50) were purchased from Taitool Bioscience Co., Ltd. (Shanghai,

428 China). *AAV9-Ef1α-DIO-H2B-EGFP* (PT-0258), *AAV9-Ef1α-DIO-EYFP* (PT-0012),
429 *AAV9-CaMKIIα-ChR2-mCherry* (PT-0297), *AAV9-VGAT2-Flp* (PT-2501, vector
430 backbone from BrainVTA), *AAV9-CCK-fDIO-mCherry* (PT-8508, vector backbone
431 from Addgene: 114471), *AAV8-Ef1α-DIO-TVA-H2B-EGFP* (PT-0021), *AAV8-Ef1α-*
432 *DIO-RVG* (PT-0023) and *RV-ENVA-ΔG-dsRed* (R01002) were purchased from
433 BrainVTA Co., Ltd. (Wuhan, China). *AAV9-PV-Flp* (BC-0430, vector backbone from
434 Addgene: 22914), *AAV9-SST-Flp* (BC-0429, vector backbone from Addgene: 22913),
435 *AAV9-Ef1α-fDIO-ChR2-mCherry* (BC-0113), *AAV9-Ef1α-fDIO-mCherry* (BC-0193)
436 and *AAV9-Ef1α-fDIO-hM3Dq-mCherry* (BC-0495) were purchased from Brain Case
437 Co., Ltd. (Shenzhen, China).

438 **Stereotaxic surgery**

439 Mice were anesthetized with 2% isoflurane and placed in a stereotaxic instrument
440 (RWD Life Science, Shenzhen, China). Microinjections were performed using 33-
441 gauge needles connected to a 10 μl microsyringe (Hamilton, Bonaduz, Switzerland),
442 which were under the control of a UMP3 ultra micropump (World Precision Instruments,
443 Florida, USA). The coordinates relative to bregma were listed as follows: anterior-
444 posterior (AP) - 1.9 mm; medial-lateral (ML) ± 1.1 mm; dorsal-ventral (DV) - 2.1 mm
445 for DG and AP - 4.7 mm; ML ± 3.2 mm; DV - 4.5 mm for MEC. The needle was slowly
446 lowered to the target site and remained for at least 3 min after injection. The injection
447 volume per site was 0.3 μl in DG and 0.4 μl in MEC. The final titer of all the AAVs
448 used for infections were at least 1×10^{12} V.G./ml except for *AAV-SST-Flp, AAV-PV-Flp,*
449 *AAV-VGAT2-Flp, AAV-Fos-RAM-d2tTA-TRE-Cre* and *AAV-Npas4-RAM-d2tTA-TRE-*

450 *Cre,* which were 1:1000 diluted. For rabies infections, the final titer used was 1×10^8
451 IFU/ml. After surgery, all mice were given at least 3 weeks to recover before behavioral
452 experiments or electrophysiological recordings, and the efficiency of virus infection
453 was verified by immunostaining. Only the mice with virus infection in correct places
454 were chosen for further analysis.

455 **Engram labeling**

456 To label engram cells, *Fos-RAM-d2tTA-TRE (F-RAM)* and *Npas4-RAM-d2tTA-TRE (N-*
457 *RAM)* systems, which gene expression was under the control of the tetracycline
458 responsive element (TRE), were used respectively through AAVs infusion. All mice
459 were kept on doxycycline (Dox, Huamaike Bio, 360304) containing food (40 mg/kg)
460 one day before virus injection. 48 hr (day -2) before engram labeling, mice were fed
461 with regular food instead of Dox diet. Then contextual fear conditioning or novel
462 context exposure (context N) was performed on day 0 to label Fos^+ or $Npas4^+$ engram
463 cells in DG, after labeling, mice were put on Dox containing food again immediately.
464 Mice were given at least 3 days to allow sufficient protein expression before subsequent
465 experiments.

466 **Rabies input tracing**

467 To study the respective monosynaptic inputs of Fos^+ and $Npas4^+$ ensembles in DG,
468 Rabies trans-synaptic tracing experiment was performed. Mice were infected with
469 *AAV_9-Fos-RAM-d2tTA-TRE-Cre* or *AAV_9-Npas4-RAM-d2tTA-TRE-Cre,* AAV helper
470 (*AAV_8-Ef1α-DIO-TVA-H2B-EGFP* and *AAV_8-Ef1α-DIO-RVG*). On day 3 after engram
471 labeling, Rabies virus (*RV-ENVA-ΔG-dsRed*) was injected into DG at the same

472 coordinates, then mice were housed in the BSL2 facility for 1 week to allow rabies
473 spread and dsRed expression before perfusion (day 10). For rabies tracing analysis,
474 consecutive brain slices from AP + 2.8 mm to AP - 5.0 mm (40 μm thickness) selected
475 from every fifth slice were collected. $DsRed^+$ cells were manually counted by an
476 experimenter who was blind to the experimental condition. The percentage of rabies-
477 labelled inputs was calculated as follows, $dsRed^+$ cells in each brain region / total
478 $dsRed^+$ cells per mouse.

479 **Contextual fear conditioning (CFC)**

480 Before CFC was performed, mice were handled daily in a holding room for 3 days. For
481 experiments with Dox-dependent ensembles labeling, on the third handling day, the
482 Dox diet was replaced with regular food (off-Dox) and CFC assay was typically carried
483 out 48 hours after the last handling session. CFC was performed in the conditioning
484 chamber (Med-Associates, St. Albans, VT, USA) and the procedure was composed of
485 conditioning and test sessions.

486 On the conditioning day (day 0), mice were firstly transported into the holding room
487 and allowed to habituate for at least 30 minutes, then transported into the behavioral
488 room and placed into context A, a square plexiglass observational chamber with
489 stainless steel bars connected to a shock generator on the floor for conditioning. Two
490 individual conditioning protocols were used in our study, for mice that conditioned to
491 the 360 s protocol, three foot shocks (0.5 mA, 1 s each) at 180 s, 240 s and 300 s were
492 given and mice were taken out 60 s after termination of the third foot shock, for mice
493 that conditioned to the180 s protocol, one single foot shock (0.3 mA, 1 s) at 120 s was

given and mice were taken out 60 s after termination of the foot shock.

The test session was carried out on day 3. Mice were put back into fear context A for 180 s, and were placed into a non-fear context (context C, a triangular chamber with white, smooth plastic floor and black cover) for 180 s 6 hr later. For immunohistochemistry, mice were tested for memory expression in only one context, either context A or C, and sacrificed 1 hr later.

The freezing percentage was automatically analyzed by software (Med-Associates) with freezing defined as absence of movement for at least 1 s. The discrimination index (DI) was calculated as follows, (the freezing percentage in context A - the freezing percentage in context C) / (the freezing percentage in context A + the freezing percentage in context C).

Open field test (OFT)

Spontaneous locomotor activity was carried out as we previously reported[39], in short, mice were placed in the center of an open arena (40 × 40 cm^2) at the beginning of the test, and were allowed to freely explore the arena for 20 min. Distance travelled in the arena and time in center zone were quantified using a TopScan automated detection system (CleverSys, Reston, VA, USA).

O-maze test

The O-maze was 70 cm in diameter and 70 cm high off the ground, and consisted of two open arms (7 cm wide) without walls, two closed arms that were enclosed by vertical walls. Mice were gently placed into the open arms, and their behavior was recorded for 6 min via a TopScan automated detection system (CleverSys, Reston, VA,

516 USA) located above the maze.

517 **Tail suspension test (TST)**

518 Mice were suspended 20 cm above a solid surface by the use of adhesive tape applied
519 to the tail, and their behavior was recorded for 6 min. Immobility time was defined as
520 absence of struggling for at least 1 s and latency to immobility was defined as the time
521 from the beginning of TST to mice's first absence of struggling for at least 1 s, which
522 were manually analyzed by an experimenter who was blind to the experimental
523 condition.

524 **Drug injections**

525 Clozapine N-oxide (CNO, Sigma, C0832) was dissolved in saline, which was
526 intraperitoneal injected (i.p.) at a concentration of 1 mg/kg 30 min before memory
527 retrieval. The KCNQ2/3 activator, retigabine (Supelco, 90221) was diluted in 5%
528 DMSO (Sigma, 276855) and administered i.p. at 1 mg/kg 30 min before memory
529 retrieval with 5% DMSO as control. 4-Hydroxytamoxifen (4-OHT, Sigma, H6278) was
530 dissolved in ethanol at 20 mg/ml and stored at -20℃. The ethanol was evaporated at
531 95℃ and corn oil (Thermo Fisher, C40543) was added to give a final concentration of
532 10 mg/ml, which was i.p. injected 2 hr before memory conditioning with corn oil as
533 control.

534 **Whole-cell patch-clamp recording in brain slices**

535 Mice were subjected to electrophysiology on day 3 following CFC. Living acute brain
536 slices (300 μm) preparation for analyzing engram synaptic connections and engram
537 intrinsic excitability were performed as previously described[40] only with minor

538 modifications. Briefly, mice's brains were cut on a vibratome (Thermo Scientific, MA,
539 USA) in carbogenated (95% O_2, 5% CO_2) ice-cold cutting solution containing (in mM):
540 93 NMDG, 2.5 KCl, 1.25 NaH_2PO_4, 30 $NaHCO_3$, 20 HEPES, 25 glucose, 2 thiourea, 5
541 Na-ascorbate, 3 Na-pyruvate, 0.5 $CaCl_2$ and 10 $MgCl_2$, 300-310 mOsm, pH adjusted to
542 7.3 with HCl. After initial recovery at 32 °C for 10 min, slices were transferred to
543 carbogenated HEPES holding ACSF (in mM: 92 NaCl, 2.5 KCl, 1.25 NaH_2PO_4, 30
544 $NaHCO_3$, 20 HEPES, 25 glucose, 2 thiourea, 5 Na-ascorbate, 3 Na-pyruvate, 2 $CaCl_2$
545 and 2 $MgCl_2$, 300-310 mOsm, pH 7.4) and incubated for over 45 min before recording.
546 Whole-cell patch-clamp recordings were performed in carbogenated recording ACSF
547 (in mM: 119 NaCl, 2.5 KCl, 1.25 NaH_2PO_4, 24 $NaHCO_3$, 12.5 glucose, 2 $CaCl_2$ and 2
548 $MgCl_2$ (300-310 mOsm, pH 7.3-7.4) at a rate of 1.5 mL / min (30~32°C) with an EPC-
549 10 amplifier and Pulse v8.78 software (HEKA Elektronik, Lambrecht/Pfalz, Germany).
550 Recording neurons were identified visually by location, morphology, size and
551 fluorescence and recordings were performed using borosilicate glass pipettes (5-7 MΩ
552 tip resistance).
553 To record A/N ratios, neurons were voltage-clamped at -70 mV to record AMPAR
554 mediated EPSCs and at +40 mV to record dual-component EPSCs containing NMDA
555 receptor (NMDAR) EPSCs. To calculate the A/N ratios, the peak current of the AMPA
556 EPSC at -70 mV was compared with the value of the NMDA EPSC after stimulation
557 start time 50 ms at +40 mV. Intracellular solution used was (in mM): 127.5 cesium
558 methanesulfonate, 7.5 CsCl, 10 HEPES, 2.5 $MgCl_2$, 4 Mg-ATP, 0.4 Na_3-GTP, 10
559 sodium phosphocreatine, 0.6 EGTA (290-300 mOsm, pH 7.2).

560 To record light-evoked EPSCs (oEPSC), A TTL-driven light-emitting diode (Lumen
561 Dynamics) was used to generate photostimulation consisting of a single wide-field blue
562 flash (470 nm, 1 ms duration) for photostimulation of ChR2-expressing terminals. The
563 laser intensity was measured at the focal plane of the slice when delivered through the
564 40× water-immersion objective lens (Nikon, Japan). Slices containing MEC ChR2-
565 expressing terminals were chosen for oEPSC recording in the presence of 1 μM
566 Tetrodotoxin (TTX, Tocris, 1078), 100 μM 4-aminopyridine (4-AP, Sigma, 275875)
567 and 100 μM picrotoxin (PTX, Tocris, 1128), neurons were voltage-clamped at -70 mV
568 and the stimulus intensity was 0.1 mW at 470 nm. To record paired-pulse ratio (PPR)
569 and AMPA/NMDA (A/N) EPSC ratio, DG slices containing ChR2-expressing neurons
570 were chosen to perform patch-clamp recordings in the presence of 100 μM PTX and
571 the stimulus intensity was 0.1 mW at 470 nm. The AMPA receptor (AMPAR) mediated
572 EPSCs were evoked by paired photostimulation of 50 ms interval for 10 consecutive
573 traces, and PPR was determined as the peak amplitude ratio of the second to the first
574 EPSC. To record light-evoked IPSCs (oIPSC) and PPR, neurons were clamped at +10
575 mV in the presence of 1 μM TTX, 100 μM 4-AP, 20 μM CNQX (Sigma, C127) and 50
576 μM D-AP5 (Tocris, 0106) and the stimulus duration and intensity was 1 ms, 0.2 mW at
577 470 nm. The recording protocols and intracellular solution used were the same as above.
578 To record Action Potentials (AP), current-clamp was used and membrane potentials
579 were measured in response to intracellular injection of step currents (1000 ms duration,
580 magnitudes ranging from - 150 to 250 pA in steps of 10 pA) with the addition of 20 μM
581 CNQX, 50 μM D-AP5 and 100 μM PTX into ACSF. Intracellular solution used was (in

582 mM): 135 potassium-gluconate, 4 KCl, 2 NaCl, 10 HEPES, 4 EGTA, 4 Mg-ATP, 0.3
583 Na3-GTP, 10 sodium phosphocreatine (280-290 mOsm, pH 7.3).
584 To record and isolate M-current (I_M), intracellular solution used was the same as above,
585 0.2 mM $CdCl_2$ (Sigma, 202908), 1 μM TTX, 10 μM ZD7288 (Tocris, 1000), and 4 mM
586 4-AP to block voltage-dependent Cav, Nav, HCN and Kv1 channels, 20 μM CNQX, 50
587 μM D-AP5 and 100 μM picrotoxin to block synaptic activity were added into ACSF.
588 To isolate M-current, the following protocol the same as previously reported[41] with
589 minor modifications was applied to the recording cells: (1) a 1 s step from the holding
590 potential (-70 mV) to -10 mV was applied to activate I_M while inactivating most other
591 voltage-gated currents, (2) a 1 s step from -60 mV to -10 mV with 10 mV increments
592 to elicit I_M tail current, and (3) a 1 s step to -10 mV, before returning to -70 mV.
593 The signals were acquired at 10 kHz and filtered at 2 kHz. The series resistance was <
594 30 MΩ. Data were analyzed with Mini Analysis Program (Synaptosoft, Fort Lee, NJ,
595 USA) or pCLAMP10.7 (Molecular Devices, San Jose, CA, USA) by an experimenter
596 who was blind to the experimental condition.

597 **Ribosome-Associated Messenger RNA Purification/ RiboTag**

598 DG from mice injected *AAV9-F/N-RAM-Cre* and *AAV9-Flex-NBL10,* Cre-dependent
599 expression of N terminus of ribosomal subunit protein Rpl10a (NBL10)[42] following
600 fear conditioning (Day 3) was quickly isolated and used for enrichment of ribosome-
601 associated transcripts as described previously[18]. The brain tissue (DG) was
602 homogenized in supplemented hybridization buffer (HB-S) containing dithiothreitol
603 (DTT, Sigma, D9760), cycloheximide (CHX, Cayman, 14126), heparin (Tocris, 2812),

604 protease inhibitors (Roche, 04693116001), and RNase inhibitor (Vazyme, R301). The
605 supernatant was incubated with anti-hemagglutinin (HA) antibody (Sigma, H6908) and
606 Dynabeads Protein G (Invitrogen, 10003D) for 12 hours. Purified messenger RNA
607 (mRNA) was eluted from the Dynabeads using TRIzol^{TM} LS (Invitrogen, 10296010).
608 An Agilent RNA 6000 Pico Kit (Agilent, 5067-1513) and an Agilent 2100 bioanalyzer
609 were used to evaluate the quality of purified mRNA. Purified mRNA samples with RNA
610 integrity number < 7 were discarded.

611 **Sequence Processing and Data Analysis**

612 The library was prepared with VAHTSTM mRNA-seq V3 Library Prep Kit for Illumina
613 (Vazyme, NR611) and sequenced on a HiSeq 4000 (Illumina) by Novogene Technology
614 Co., Ltd (Beijing, China). Raw reads were cleaned with FASTX-toolkit to remove
615 adapter contamination and low-quality reads (quality score < 28). The clipped reads
616 were aligned to mouse reference sequence (GRCm38/mm10) using HISAT2[43].
617 Cuffdiff-generated FPKM count matrix was used for subsequent analysis. Significance
618 was drawn with ANOVA and clustered using Shannon entropy-based method[44]. Genes
619 with more than one and half fold expression changes, and were significantly different
620 ($P < 0.05$) were selected for further analysis.

621 **Single molecule fluorescent in situ hybridization (smFISH)**

622 Fixed-frozen brain tissues were sliced into 10 μm coronal sections and baked at 60ºC
623 for 30 min. Then slices were incubated with hydrogen peroxide (H_2O_2) for 10 min at
624 room temperature (RT), targets retrieval and protease III incubation were performed
625 using RNAscope® 2.5 Universal Pretreatment Reagents (Advanced Cell Diagnostics,

626 322000, 322381). SmFISH probes for all genes examined: *Nptx1* (505421), *Nptx2*
627 (316901), *Fos* (316921), *Npas4* (423431), *Sirt1* (418341) and *Atg7* (561261) were
628 hybridized for 2 hr. After Hybridization, RNAscope® Multiplex Fluorescent Detection
629 Kit v2 (Advanced Cell Diagnostics, 323110) were used to amplify signals. Images were
630 acquired by using the Nikon A1 confocal microscope (Tokyo, Japan). Regions of
631 interest (ROI) were circled and the intensity within the regions was analyzed by Image-
632 Pro Plus 6.0 (Media Cybernetics, Rockville, MD, USA). For cell counting analysis,
633 consecutive brain slices from AP – 1.2 mm to AP – 2.0 mm (10 μm thickness) selected
634 from every tenth slice, 8 slices per mouse were collected, number of mice were included
635 in the statistical table.

636 **Immunohistochemistry (IHC)**

637 Mice were perfused transcardially with ice cold saline followed by 4%
638 paraformaldehyde (PFA, dissolved in 0.1 M PBS). The brains were removed and fixed
639 in 4% PFA overnight. Then the brains were subjected to dehydrate in 30% sucrose
640 solutions at 4°C for 72 hr before being sliced into 30 or 40 μm coronal sections (selected
641 from every fifth slice). Slices were incubated with primary antibodies in blocking
642 solution containing 0.3% Triton X-100 overnight at 4ºC. Slices were washed with 0.1
643 M PBS, and then incubated with secondary antibody at RT for 1.5 hr. After being
644 washed in PBS, slices were mounted in anti-quenching mounting medium (Southern
645 Biotech, 0100). Primary antibodies used were: anti-NPTX1 (1:400, Alomone Labs,
646 ANR-191), anti-NPTX2 (1:500, Proteintech, 10889-1-AP), anti-Fos (1:500, Synaptic
647 Systems, 226017), anti-Parvalbumin (PV, 1:100, Thermo Fisher, PA1-933), anti-PV

648 (1:500, Oasis, OB-PGP005-01), anti-GluA4 (1:500, Merck, AB1508), anti-
649 Somatostatin (SST, 1:200, Oasis, OB-PRB111-01), anti-Choline Acetyltransferase
650 (ChAT, 1:100, Merck, AB143), anti-Glutamate (1:500, Merck, AB133), anti-GAD67
651 (1:500, Merck, MAB5406), anti-cholecystokinin (CCK, 1:1000, Merck, C2581) and
652 anti-KCNQ2 (1:100, Alomone Labs, APC-050). Secondary antibodies used were: goat
653 anti-rat 488 (1:1000, Jackson Immuno Research, 112-545-167), goat anti-rabbit 488
654 (1:1000, Jackson Immuno Research, 111-545-144), donkey anti-guinea pig 488 (1:1000,
655 Jackson Immuno Research, 706-545-148), goat anti-rabbit Cy3 (1:1000, Jackson
656 Immuno Research, 111-165-144), donkey anti-rat Cy3 (1:1000, Jackson Immuno
657 Research, 712-165-153) and donkey anti-rat 647 (1:500, Jackson Immuno Research,
658 712-605-150). Kv7.2 and GluA4 membrane expression analysis were adapted from one
659 of the latest researches from our lab[45]. Images were acquired using a Nikon-A1 confocal
660 microscope (Tokyo, Japan) with a 20× objective lens or a 60× objective oil lens. Data
661 were analyzed blindly to the group using Image-Pro Plus 6.0 and ImageJ (Fiji). For cell
662 counting analysis, consecutive brain slices from AP – 1.2 mm to AP – 2.0 mm (40 μm
663 thickness) selected from every fifth slice, 4 slices per mouse were collected, number of
664 mice were included in the statistical table.

665 **Reverse transcription-quantitative PCR (RT-qPCR)**

666 Reverse transcription was completed using HiScript II 1st Strand cDNA Synthesis Kit
667 (Vazyme, R212). The cDNA was subjected to qPCR using ChamQ Universal SYBR
668 qPCR Master Mix (Vazyme, Q711) and Eppendorf Mastercycler PCR System. The
669 primers for qPCR were as follows: 5' - ACCTCCCTACACCAACGGAT - 3' and 5' -

670 GGCAGGCTCTTCTTCACCTT - 3' for *Nptx1*, 5' - GCCAAGGTGAAGAAGAGCCT
671 - 3' and 5' - AGCATAAGAGAAGGGTGTGCC - 3' for *Nptx1* of exon 3, 5' -
672 GACTTCCGAGAGGTGCTCCA - 3' and 5' - GGTGAGCCGAGGTCTCATTA - 3' for
673 *Nptx2* of exon 2, 5' - TGGCCTTCCGTGTTCCTAC - 3' and 5' -
674 GAGTTGCTGTTGAAGTCGCA - 3' for *Gapdh*, which were synthesized by Azenta
675 US, Inc.. The mRNA expression of *Nptx1* and *Nptx2* was normalized to the internal
676 control *Gapdh*.

677 **Co-immunoprecipitation (Co-IP) and Western blotting**

678 The DG tissues of adult C57BL/6J male mice were rapidly extracted and homogenized
679 in radio immunoprecipitation assay (RIPA) buffer containing protease and phosphatase
680 inhibitors for 30 min. The protein lysate concentration was determined using
681 bicinchoninic acid kit. Protein samples were incubated with 3 μg anti-NPTX1 (Santa
682 Cruz Biotechnology, sc-374199) or anti-IgG (Cell Signaling Technology, 5415S) for 4
683 h at 4ºC. Pierce Protein A/G magnetic beads (88803, Thermo Scientific) were added to
684 each sample and the mixture was rotated at 4°C overnight. The attached protein lysis
685 was then eluted and used for further protein blotting assay. Before Western blotting
686 assay, 50 μg protein samples were boiled for 6 min at 85ºC, and were separated by SDS-
687 polyacrylamide gel electrophoresis (PAGE) under 120 V for 1.5 h. Proteins were then
688 transferred to the polyvinylidene fluoride (PVDF) membrane at 100 mV for 100 min.
689 The membrane was firstly washed with Tris-buffered saline with Tween 20 (TBST),
690 followed by blocking in 5% skimmed milk for 2 hours. The membrane was then
691 incubated with the following primary antibodies anti-NPTX1 (1:100, Santa Cruz

692 Biotechnology, sc-374199) and anti-KCNQ2 (1:500, Abcam, ab22897) at 4°C
693 overnight. On the next day, the membrane was washed with TBST and incubated with
694 IRDye 700DX- or 800DX-conjugated anti-rabbit or anti-mouse IgG (1:50000,
695 Rockland Immunochemicals Inc.) for 2 h at room temperature. Protein bands were
696 visualized using Odyssey (LI-COR Biosciences). The immunoblots were analyzed with
697 Image J.

698 **Statistics**

699 All data were presented as mean ± SEM. Sample sizes were based on our previous
700 research[18,39,46]. Statistical analyses were performed by SPSS 20.0 software (IBM,
701 Armonk, NY, USA) or R software (version 4.1.2). The normality test of the data sets
702 was performed by the Shapiro-Wilk test or the Kolmogorov-Smirnov test if $n > 50$,
703 homogeneity of variance test of the data sets was performed by the Levene's test. Two-
704 tailed unpaired *t* test was used for comparing two independent groups. Multiple group
705 comparisons were assessed using One-way analysis of variance (ANOVA), Two-way
706 ANOVA or Two-way repeated measures (RM) ANOVA, followed by the Bonferroni's
707 post-hoc test when significant main effects or interactions were detected. Mann-
708 Whitney *U* test or Kruskal-Wallis H test was used when normality was violated.
709 Bonferroni's corrections were applied to assess statistical significance.* $P < 0.05$, ** P
710 < 0.01, and *** $P < 0.001$.

References

1. Josselyn, S. A. & Tonegawa, S. Memory engrams: Recalling the past and imagining the future. *Science* **367** (2020).
2. Tonegawa, S., Morrissey, M. D. & Kitamura, T. The role of engram cells in the systems consolidation of memory. *Nature Reviews Neuroscience* **19**, 485-498 (2018).
3. Castello-Waldow, T. P. *et al.* Hippocampal neurons with stable excitatory connectivity become part of neuronal representations. *Plos Biol* **18** (2020).
4. Luo, L. & Craik, F. I. Aging and memory: a cognitive approach. *Can J Psychiatry* **53**, 346-353 (2008).
5. Fan, X., Wheatley, E. G. & Villeda, S. A. Mechanisms of Hippocampal Aging and the Potential for Rejuvenation. *Annu Rev Neurosci* **40**, 251-272 (2017).
6. Sudhof, T. C. Towards an Understanding of Synapse Formation. *Neuron* **100**, 276-293 (2018).
7. Gomez de San Jose, N. *et al.* Neuronal pentraxins as biomarkers of synaptic activity: from physiological functions to pathological changes in neurodegeneration. *J Neural Transm (Vienna)* **129**, 207-230 (2022).
8. Cho, R. W. *et al.* mGluR1/5-dependent long-term depression requires the regulated ectodomain cleavage of neuronal pentraxin NPR by TACE. *Neuron* **57**, 858-871 (2008).
9. Xu, D. *et al.* Narp and NP1 form heterocomplexes that function in developmental and activity-dependent synaptic plasticity. *Neuron* **39**, 513-528 (2003).
10. Abad, M. A., Enguita, M., DeGregorio-Rocasolano, N., Ferrer, I. & Trullas, R. Neuronal pentraxin 1 contributes to the neuronal damage evoked by amyloid-beta and is overexpressed in dystrophic neurites in Alzheimer's brain. *J Neurosci* **26**, 12735-12747 (2006).
11. Figueiro-Silva, J. *et al.* Neuronal pentraxin 1 negatively regulates excitatory synapse density and synaptic plasticity. *J Neurosci* **35**, 5504-5521 (2015).
12. Chang, M. C. *et al.* Narp regulates homeostatic scaling of excitatory synapses on parvalbumin-expressing interneurons. *Nat Neurosci* **13**, 1090-1097 (2010).
13. Gu, Y. *et al.* Obligatory Role for the Immediate Early Gene NARP in Critical Period Plasticity. *Neuron* **79**, 335-346 (2013).
14. Xiao, M. F. *et al.* A biomarker-authenticated model of schizophrenia implicating NPTX2 loss of function. *Sci Adv* **7**, eabf6935 (2021).
15. Mravinacová, S. *et al.* CSF protein ratios with enhanced potential to reflect Alzheimer's disease pathology and neurodegeneration. *Mol Neurodegener* **19** (2024).
16. Soldan, A. *et al.* NPTX2 in Cerebrospinal Fluid Predicts the Progression From Normal Cognition to Mild Cognitive Impairment. *Ann Neurol* **94**, 620-631 (2023).
17. Sun, X. *et al.* Functionally Distinct Neuronal Ensembles within the Memory Engram. *Cell* **181**, 410-423 e417 (2020).
18. Wang, Z. *et al.* Retrieval-Driven Hippocampal NPTX2 Plasticity Facilitates the Extinction of Cocaine-Associated Context Memory. *Biol Psychiatry* **87**, 979-991 (2020).
19. Mariga, A. *et al.* Definition of a Bidirectional Activity-Dependent Pathway Involving BDNF and Narp. *Cell Rep* **13**, 1747-1756 (2015).
20. Delmas, P. & Brown, D. A. Pathways modulating neural KCNQ/M (Kv7) potassium channels.

754 *Nat Rev Neurosci* **6**, 850-862 (2005).
755 21. Li, S. B. *et al.* Hyperexcitable arousal circuits drive sleep instability during aging. *Science*
756 **375**, eabh3021 (2022).
757 22. Topolnik, L. & Tamboli, S. The role of inhibitory circuits in hippocampal memory
758 processing. *Nat Rev Neurosci* **23**, 476-492 (2022).
759 23. Royer, S. *et al.* Control of timing, rate and bursts of hippocampal place cells by dendritic
760 and somatic inhibition. *Nat Neurosci* **15**, 769-775 (2012).
761 24. Cummings, D. M. *et al.* Neuronal and Peripheral Pentraxins Modify Glutamate Release and
762 may Interact in Blood-Brain Barrier Failure. *Cereb Cortex* **27**, 3437-3448 (2017).
763 25. Pelkey, K. A. *et al.* Pentraxins Coordinate Excitatory Synapse Maturation and Circuit
764 Integration of Parvalbumin Interneurons. *Neuron* **90**, 661 (2016).
765 26. Blackburn-Munro, G., Dalby-Brown, W., Mirza, N. R., Mikkelsen, J. D. & Blackburn-Munro,
766 R. E. Retigabine: chemical synthesis to clinical application. *CNS Drug Rev* **11**, 1-20 (2005).
767 27. Bieri, G., Schroer, A. B. & Villeda, S. A. Blood-to-brain communication in aging and
768 rejuvenation. *Nat Neurosci* **26**, 379-393 (2023).
769 28. Regev, N. *et al.* Selective interaction of syntaxin 1A with KCNQ2: possible implications for
770 specific modulation of presynaptic activity. *PLoS One* **4**, e6586 (2009).
771 29. Luna, V. M. *et al.* Adult-born hippocampal neurons bidirectionally modulate entorhinal
772 inputs into the dentate gyrus. *Science* **364**, 578-583 (2019).
773 30. Qin, H. *et al.* A Visual-Cue-Dependent Memory Circuit for Place Navigation. *Neuron* **99**,
774 47-55 e44 (2018).
775 31. Bartos, M. & Elgueta, C. Functional characteristics of parvalbumin- and cholecystokinin-
776 expressing basket cells. *J Physiol* **590**, 669-681 (2012).
777 32. Klausberger, T. *et al.* Complementary roles of cholecystokinin- and parvalbumin-
778 expressing GABAergic neurons in hippocampal network oscillations. *J Neurosci* **25**, 9782-
779 9793 (2005).
780 33. Sun, X. & Lin, Y. Npas4: Linking Neuronal Activity to Memory. *Trends Neurosci* **39**, 264-
781 275 (2016).
782 34. Spiegel, I. *et al.* Npas4 regulates excitatory-inhibitory balance within neural circuits
783 through cell-type-specific gene programs. *Cell* **157**, 1216-1229 (2014).
784 35. Pollina, E. A. *et al.* A NPAS4-NuA4 complex couples synaptic activity to DNA repair. *Nature*
785 **614**, 732-741 (2023).
786 36. Bloodgood, B. L., Sharma, N., Browne, H. A., Trepman, A. Z. & Greenberg, M. E. The
787 activity-dependent transcription factor NPAS4 regulates domain-specific inhibition.
788 *Nature* **503**, 121-125 (2013).
789 37. Yap, E. L. *et al.* Bidirectional perisomatic inhibitory plasticity of a Fos neuronal network.
790 *Nature* **590**, 115-121 (2021).
791 38. Ramsaran, A. I. *et al.* A shift in the mechanisms controlling hippocampal engram formation
792 during brain maturation. *Science* **380**, 543-551 (2023).
793 39. Jin, T. *et al.* Dorsal hippocampus- and ACC-projecting medial septum neurons
794 differentially contribute to the recollection of episodic-like memory. *FASEB J* **34**, 11741-
795 11753 (2020).
796 40. Ting, J. T., Daigle, T. L., Chen, Q. & Feng, G. Acute brain slice methods for adult and aging
797 animals: application of targeted patch clamp analysis and optogenetics. *Methods Mol Biol*

1183, 221-242 (2014).

41. Lopez, J. P. *et al.* Ketamine exerts its sustained antidepressant effects via cell-type-specific regulation of Kcnq2. *Neuron* **110**, 2283-2298 e2289 (2022).

42. Ekstrand, M. I. *et al.* Molecular profiling of neurons based on connectivity. *Cell* **157**, 1230-1242 (2014).

43. Kim, D., Paggi, J. M., Park, C., Bennett, C. & Salzberg, S. L. Graph-based genome alignment and genotyping with HISAT2 and HISAT-genotype. *Nat Biotechnol* **37**, 907-915 (2019).

44. Ghosh, S. & Chan, C. K. Analysis of RNA-Seq Data Using TopHat and Cufflinks. *Methods Mol Biol* **1374**, 339-361 (2016).

45. He, G. *et al.* Persistent increase of accumbens cocaine ensemble excitability induced by IRK downregulation after withdrawal mediates the incubation of cocaine craving. *Mol Psychiatry* **28**, 448-462 (2023).

46. Zhou, Y. *et al.* A ventral CA1 to nucleus accumbens core engram circuit mediates conditioned place preference for cocaine. *Nat Neurosci* **22**, 1986-1999 (2019).

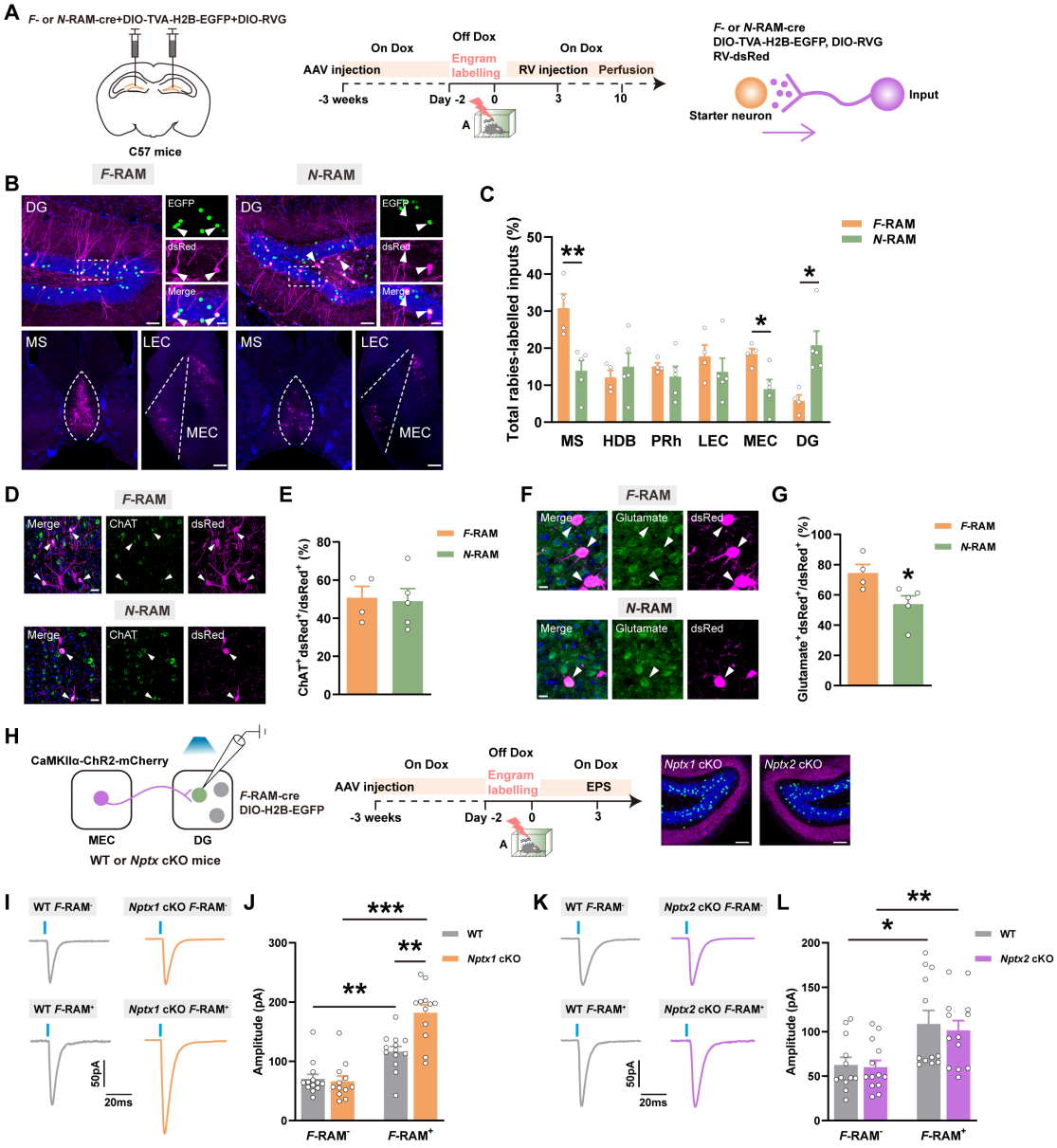
A
F- or N-RAM-cre+DIO-TVA-H2B-EGFP+DIO-RVG
C57 mice
On Dox
Off Dox
On Dox
AAV injection
Engram labelling
RV injection
Perfusion
-3 weeks
Day -2
0
3
10
F- or N-RAM-cre
DIO-TVA-H2B-EGFP, DIO-RVG
RV-dsRed
Starter neuron
Input
B
F-RAM
N-RAM
DG
EGFP
dsRed
Merge
MS
LEC
MEC
C
Total rabies-labelled inputs (%)
F-RAM
N-RAM
MS
HDB
PRh
LEC
MEC
DG
D
F-RAM
N-RAM
Merge
ChAT
dsRed
E
ChAT+dsRed+/dsRed+ (%)
F
Glutamate
G
Glutamate+dsRed+/dsRed+ (%)
H
CaMKIIα-ChR2-mCherry
F-RAM-cre
DIO-H2B-EGFP
MEC
DG
WT or Nptx cKO mice
EPS
Nptx1 cKO
Nptx2 cKO
I
WT F-RAM-
Nptx1 cKO F-RAM-
WT F-RAM+
Nptx1 cKO F-RAM+
50pA
20ms
J
Amplitude (pA)
WT
Nptx1 cKO
F-RAM-
F-RAM+
K
WT F-RAM-
Nptx2 cKO F-RAM-
WT F-RAM+
Nptx2 cKO F-RAM+
L
Nptx2 cKO

Figure 1. Rabies virus tracing of the upstream inputs to DG *F*- and *N*-RAM neuronal ensembles and the effects of *Nptxs* depletion on response to MEC excitatory inputs. (A) Diagram of virus injection and experimental scheme to trace upstream inputs of DG *F*-RAM and *N*-RAM ensembles. (B) Representative confocal images of DG starter neurons in *F*-RAM, *N*-RAM ensembles and their respective upstream inputs. Green: *F*-RAM or *N*-RAM engram cells, EGFP, Purple: dsRed, Blue: DAPI. White arrows indicate the starter neurons and DG local inputs. Scale bar: top left, 50 μm, top right, 10 μm, bottom, 100 μm. (C) The percentages of total inputs from each upstream site relative to total quantified inputs. (D) Representative confocal images of upstream MS $dsRed^+$ cells immunostaining with ChAT. Green: ChAT, Purple: dsRed, Blue: DAPI. White arrows indicate the colocalized cells. Scale bar: 10 μm. (E) The percentages of colocalized cells in MS total $dsRed^+$ cells. (F) Representative confocal images of upstream MEC $dsRed^+$ cells immunostaining with glutamate. Green: glutamate, Purple: dsRed, Blue: DAPI. White arrows indicate the colocalized cells. Scale bar: 5 μm. (G) The percentages of colocalized cells in MEC total $dsRed^+$ cells. (H) Diagram of AAV injection, experimental scheme and representative expression of ChR2 in MEC projection neurons and DG engram cells. Green: *F*-RAM engram cells of *Nptx1* and *Nptx2* cKO mice, EGFP, Purple: MEC projections, mCherry, Blue: DAPI. Scale bar: 50 μm. (I, K) Representative traces of oEPSC recorded from WT and *Nptxs* cKO mice. (J) The quantification of oEPSC amplitudes recorded from WT and *Nptx1* cKO mice. (L) The quantification of oEPSC amplitudes recorded from WT and *Nptx2* cKO mice. Data are presented as mean ± S.E.M; $*P < 0.05$, $**P < 0.01$, $***P < 0.001$.

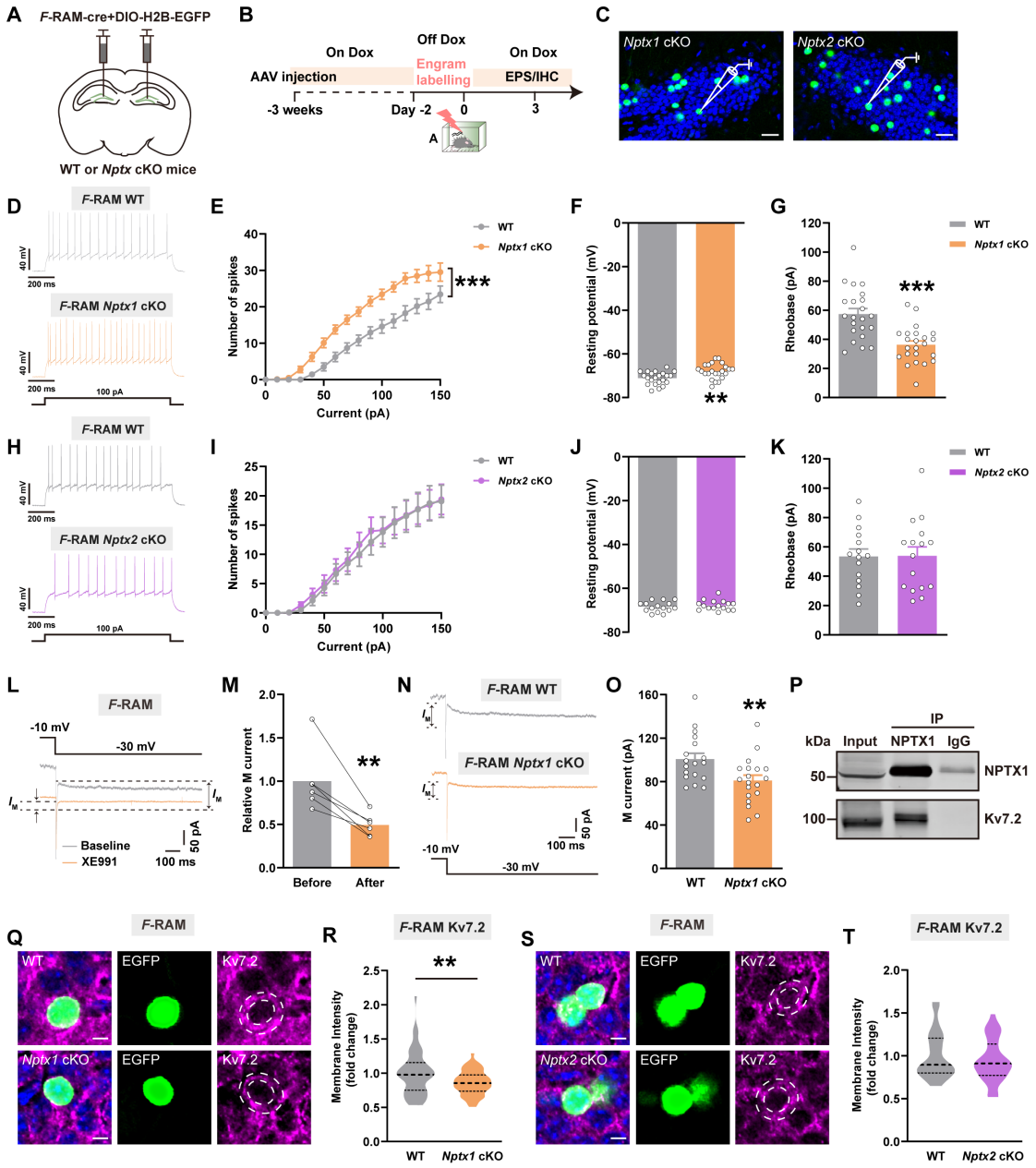
A
F-RAM-cre+DIO-H2B-EGFP
WT or Nptx cKO mice
B
On Dox
Off Dox
On Dox
AAV injection
Engram labelling
EPS/IHC
-3 weeks
Day -2
0
3
C
Nptx1 cKO
Nptx2 cKO
D
F-RAM WT
F-RAM Nptx1 cKO
E
Number of spikes
Current (pA)
WT
Nptx1 cKO
***
F
Resting potential (mV)
**
G
Rheobase (pA)
***
H
F-RAM WT
F-RAM Nptx2 cKO
I
Number of spikes
Current (pA)
WT
Nptx2 cKO
J
Resting potential (mV)
K
Rheobase (pA)
L
F-RAM
-10 mV
-30 mV
Baseline
XE991
50 pA
100 ms
M
Relative M current
**
Before
After
N
F-RAM WT
F-RAM Nptx1 cKO
-10 mV
-30 mV
100 ms
50 pA
O
M current (pA)
**
WT
Nptx1 cKO
P
kDa
Input
IP
NPTX1
IgG
50
100
NPTX1
Kv7.2
Q
F-RAM
WT
EGFP
Kv7.2
Nptx1 cKO
R
F-RAM Kv7.2
**
Membrane Intensity (fold change)
WT
Nptx1 cKO
S
F-RAM
Nptx2 cKO
T
F-RAM Kv7.2
Membrane Intensity (fold change)
WT
Nptx2 cKO

838

839

840 **Figure 2. The effects of *Nptx1* or *Nptx2* depletion on engram excitability and**
841 **membrane expression of Kv7.2.** (A) Diagram of AAV injection. (B) Experimental
842 scheme to label *F*-RAM, *N*-RAM engram ensembles. EPS: Electrophysiology, IHC:
843 Immunohistochemistry. (C) Representative expression of *F*-RAM engram cells in DG
844 of *Nptx1* and *Nptx2* cKO mice. Green: *F*-RAM engram cells of *Nptx1* and *Nptx2* cKO
845 mice, EGFP, Blue: DAPI. Scale bar: 20 μm. (D, H) Representative AP traces induced
846 by depolarizing current injections (100 pA) recorded from WT and *Nptxs* cKO mice.
847 (E) The input-output curves of AP spikes versus injected currents of WT and *Nptx1*
848 cKO mice. (F) The RMP of WT and *Nptx1* cKO mice. (G) The rheobase of WT and
849 *Nptx1* cKO mice. (I) The input-output curves of AP spikes versus injected currents of
850 WT and *Nptx2* cKO mice. (J) The RMP of WT and *Nptx2* cKO mice. (K) The rheobase
851 of WT and *Nptx2* cKO mice. (L) Representative traces of I_M current recorded before
852 and after application of XE991. (M) The normalized I_M current recorded at -30 mV
853 before and after application of XE991. (N) Representative traces of I_M current recorded
854 from WT and *Nptx1* cKO mice. (O) The average I_M current amplitudes recorded at -30
855 mV from WT and *Nptx1* cKO mice. (P) Immunoblotting of NPTX1 co-
856 immunoprecipitates with Kv7.2 in DG. (Q, S) Representative confocal images of
857 engram cells colocalizing with Kv7.2. Green: *F*-RAM engram cells, EGFP, Purple:
858 Kv7.2, Blue: DAPI. Dashed white lines outline cell membrane. Scale bar: 5 μm. (R)
859 The quantification of membrane Kv7.2 fluorescence intensity of WT and *Nptx1* cKO
860 neurons. (T) The quantification of Kv7.2 fluorescence intensity of WT and *Nptx2* cKO
861 neurons. Data are presented as mean ± S.E.M; $^{**}P < 0.01$, $^{***}P < 0.001$.
862

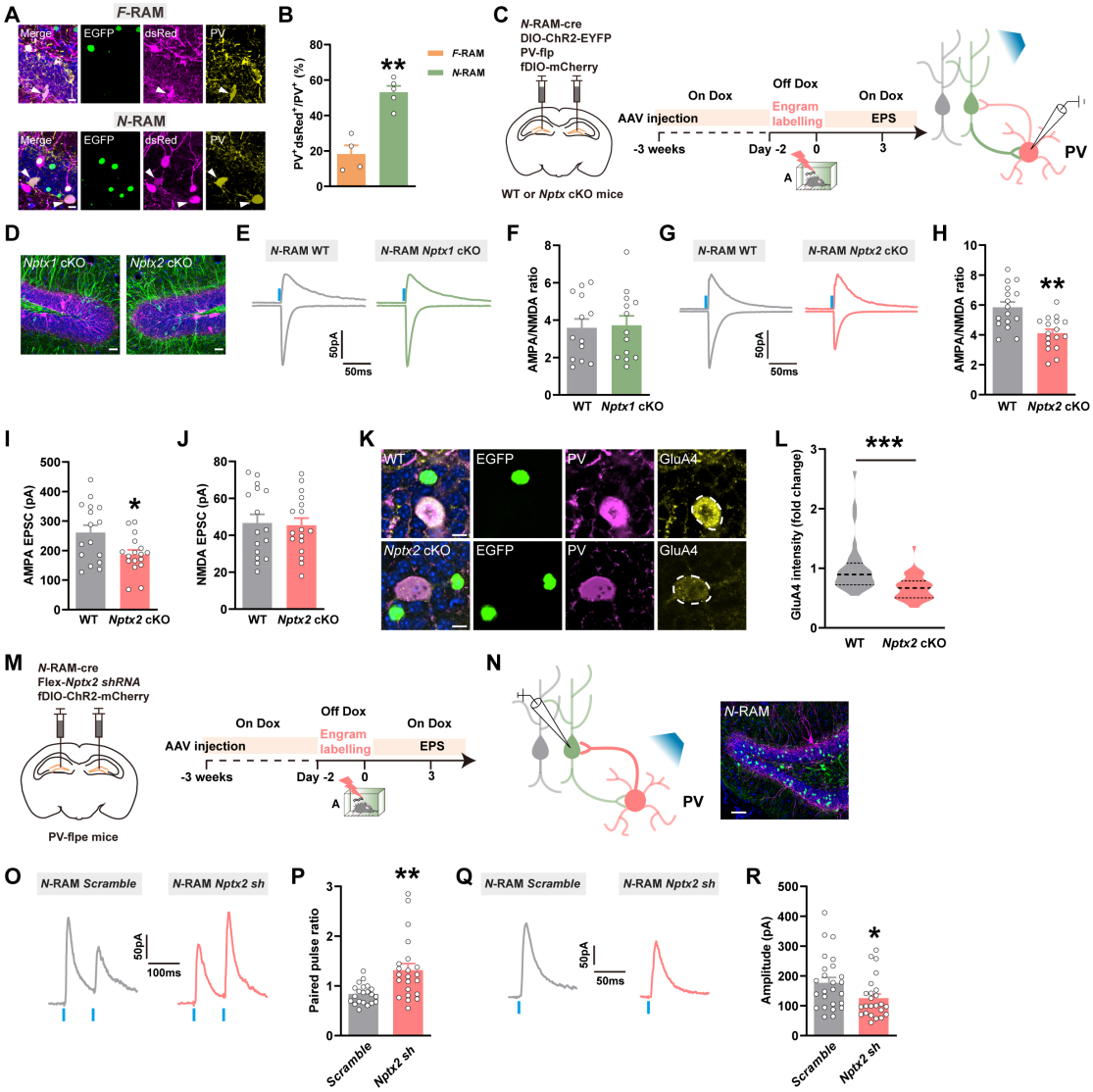
A
F-RAM
Merge
EGFP
dsRed
PV
N-RAM
B
PV+dsRed+/PV+ (%)
F-RAM
N-RAM
C
N-RAM-cre
DIO-ChR2-EYFP
PV-flp
fDIO-mCherry
WT or Nptx cKO mice
AAV injection
On Dox
Off Dox
Engram labelling
On Dox
EPS
-3 weeks
Day -2
0
3
PV
D
Nptx1 cKO
Nptx2 cKO
E
N-RAM WT
N-RAM Nptx1 cKO
50pA
50ms
F
AMPA/NMDA ratio
WT
Nptx1 cKO
G
N-RAM WT
N-RAM Nptx2 cKO
H
AMPA/NMDA ratio
WT
Nptx2 cKO
I
AMPA EPSC (pA)
WT
Nptx2 cKO
J
NMDA EPSC (pA)
WT
Nptx2 cKO
K
WT
EGFP
PV
GluA4
Nptx2 cKO
L
GluA4 intensity (fold change)
WT
Nptx2 cKO
M
N-RAM-cre
Flex-Nptx2 shRNA
fDIO-ChR2-mCherry
PV-flpe mice
N
PV
N-RAM
O
N-RAM Scramble
N-RAM Nptx2 sh
50pA
100ms
P
Paired pulse ratio
Scramble
Nptx2 sh
Q
N-RAM Scramble
N-RAM Nptx2 sh
50pA
50ms
R
Amplitude (pA)
Scramble
Nptx2 sh

865 **Figure 3. The effects of *Nptx2* depletion on the functional connection between DG**
866 **local PV$^+$ interneurons and *N*-RAM ensemble.** (A) Representative confocal images
867 of DG local dsRed$^+$ cells immunostaining with PV. Green: EGFP, Purple: dsRed,
868 Yellow: PV, Blue: DAPI. White arrows indicate the dsRed$^+$ PV$^+$ colocalized cells. Scale
869 bar: 5 μm. (B) The percentages of colocalized cells in DG total PV$^+$ cells. (C) Diagram
870 of AAV injection and experimental scheme to label *N*-RAM engram ensembles. (D)
871 Diagram of representative expression of engram cells and PV$^+$ interneurons. Green: *N*-
872 RAM engram cells of *Nptx1* and *Nptx2* cKO mice, EYFP, Purple: PV$^+$ interneurons,
873 mCherry, Blue: DAPI. Scale bar: 10 μm. (E, G) Representative traces of opto-evoked
874 AMPA-EPSC and NMDA-EPSC recorded from WT and *Nptxs* cKO mice. (F) The
875 average A/N ratio recorded from WT and *Nptx1* cKO mice. (H) The average A/N ratio
876 recorded from WT and *Nptx2* cKO mice. (I, J) The average AMPA-EPSC and NMDA-
877 EPSC amplitudes recorded from WT and *Nptx2* cKO mice. (K) Representative confocal
878 images of GluA4 colocalizing with PV$^+$ interneurons. Green: *N*-RAM engram cells,
879 Purple: PV$^+$ interneurons, Yellow: GluA4. Scale bar: 10 μm. (L) The quantification of
880 GluA4 membrane expression on PV$^+$ interneurons in WT and *Nptx2* cKO mice. (M)
881 Diagram of AAV injection and experimental scheme to label *N*-RAM engram ensemble.
882 (N) Diagram of photostimulation and whole-cell patch clamp recordings (left) and
883 representative expression of *N*-RAM engram cells and PV$^+$ interneurons (right). Green:
884 *N*-RAM engram cells, EGFP, Purple: PV$^+$ interneurons, mCherry, Blue: DAPI. Scale
885 bar: 20 μm. (O, Q) Representative traces of opto-evoked PPR and oIPSC recorded from
886 *Scramble* and *Nptx2 shRNA* neurons. (P, R) The quantification of PPR and oIPSC

887 amplitudes recorded from *Scramble* and *Nptx2 shRNA* neurons. Data are presented as

888 mean ± S.E.M; *$P < 0.05$, **$P < 0.01$, ***$P < 0.001$.

889

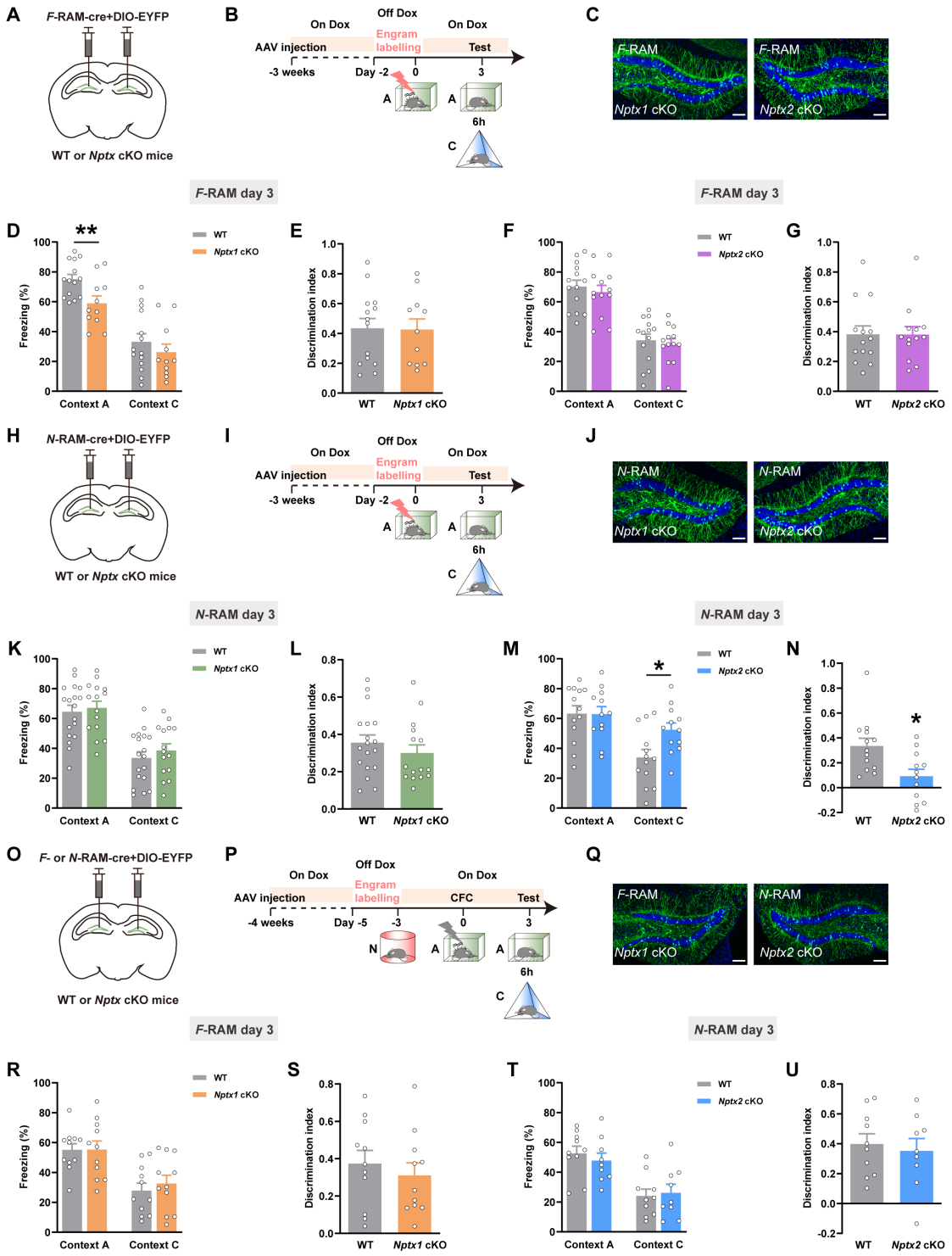
A
F-RAM-cre+DIO-EYFP
WT or Nptx cKO mice
B
On Dox
Off Dox
On Dox
AAV injection
Engram labelling
Test
-3 weeks
Day -2
0
3
A
A
6h
C
C
F-RAM
Nptx1 cKO
F-RAM
Nptx2 cKO
F-RAM day 3
F-RAM day 3
D
**
WT
Nptx1 cKO
Freezing (%)
Context A
Context C
E
Discrimination index
WT
Nptx1 cKO
F
WT
Nptx2 cKO
Freezing (%)
Context A
Context C
G
Discrimination index
WT
Nptx2 cKO
H
N-RAM-cre+DIO-EYFP
WT or Nptx cKO mice
I
On Dox
Off Dox
On Dox
AAV injection
Engram labelling
Test
-3 weeks
Day -2
0
3
A
A
6h
C
J
N-RAM
Nptx1 cKO
N-RAM
Nptx2 cKO
N-RAM day 3
N-RAM day 3
K
WT
Nptx1 cKO
Freezing (%)
Context A
Context C
L
Discrimination index
WT
Nptx1 cKO
M
*
WT
Nptx2 cKO
Freezing (%)
Context A
Context C
N
*
Discrimination index
WT
Nptx2 cKO
O
F- or N-RAM-cre+DIO-EYFP
WT or Nptx cKO mice
P
On Dox
Off Dox
On Dox
AAV injection
Engram labelling
CFC
Test
-4 weeks
Day -5
-3
0
3
N
A
A
6h
C
Q
F-RAM
Nptx1 cKO
N-RAM
Nptx2 cKO
F-RAM day 3
N-RAM day 3
R
WT
Nptx1 cKO
Freezing (%)
Context A
Context C
S
Discrimination index
WT
Nptx1 cKO
T
WT
Nptx2 cKO
Freezing (%)
Context A
Context C
U
Discrimination index
WT
Nptx2 cKO

890

891

892 **Figure 4. The effects of *Nptxs* depletion in *F*-RAM and *N*-RAM ensembles on the**
893 **expression of contextual fear memory.** (A, H, O) Diagram of AAV injection. (B, I, P)
894 Experimental scheme of CFC and memory retrieval. (C, J, Q) Representative
895 expression of *F*- and *N*-RAM engram cells in DG. Green: *F*-RAM or *N*-RAM ensemble,
896 EYFP, Blue: DAPI. Scale bar: 100 μm. (D, E) The freezing percentage and
897 discrimination index of WT and *Nptx1* cKO mice tested in context A and context C at
898 day 3 (*F*-RAM). (F, G) The freezing percentage and discrimination index of WT and
899 *Nptx2* cKO mice tested in context A and context C at day 3 (*F*-RAM). (K, L) The
900 freezing percentage and discrimination index of WT and *Nptx1* cKO mice tested in
901 context A and context C at day 3 (*N*-RAM). (M, N) The freezing percentage and
902 discrimination index of WT and *Nptx2* cKO mice tested in context A and context C at
903 day 3 (*N*-RAM). (R, S) The freezing percentage and discrimination index of WT and
904 *Nptx1* cKO mice tested in context A and context C at day 3 (*F*-RAM). (T, U) The
905 freezing percentage and discrimination index of WT and *Nptx2* cKO mice tested in
906 context A and context C at day 3 (*N*-RAM). Data are presented as mean ± S.E.M; *$P <$
907 0.05, **$P < 0.01$.
908

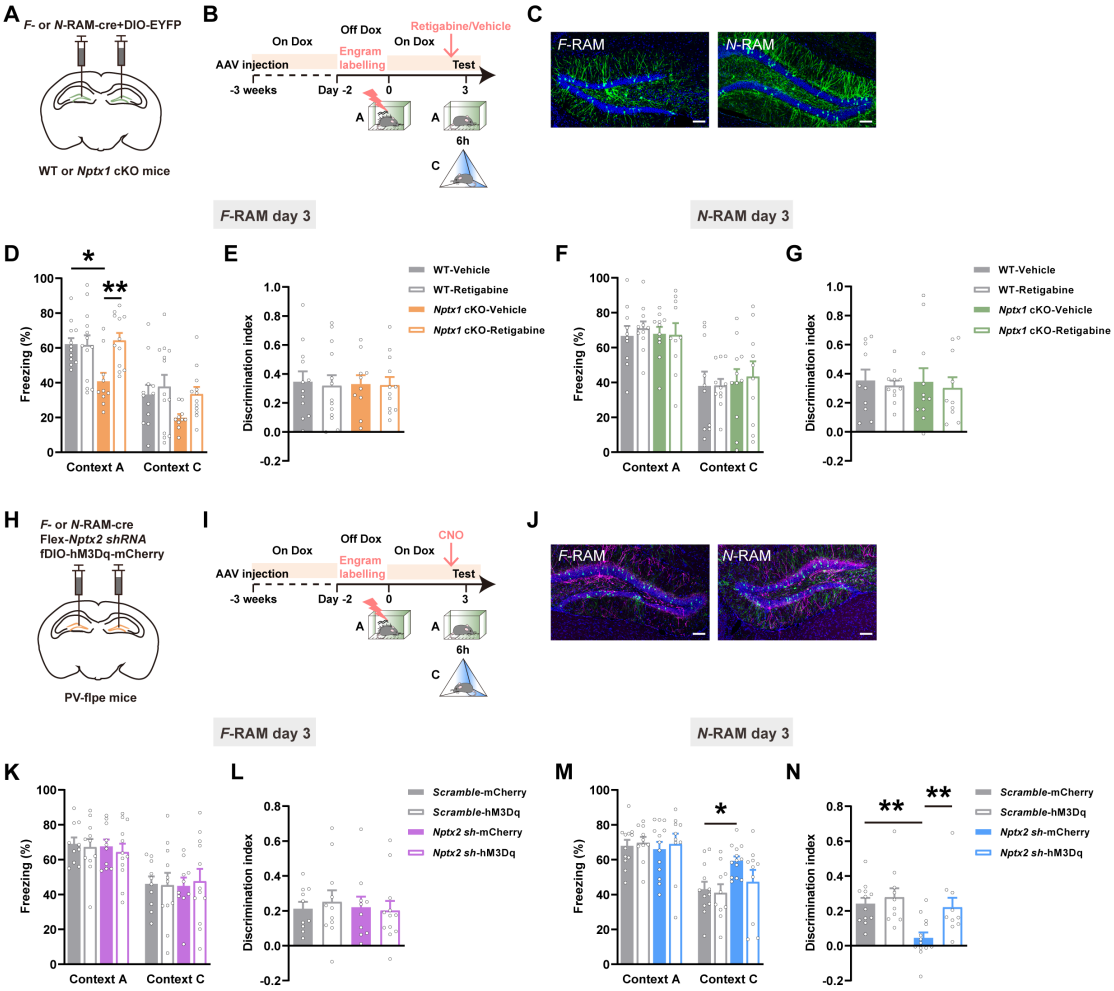
A
F- or N-RAM-cre+DIO-EYFP
WT or Nptx1 cKO mice
B
On Dox
Off Dox
Retigabine/Vehicle
On Dox
AAV injection
Engram labelling
Test
-3 weeks
Day -2
0
3
A
A
6h
C
C
F-RAM
N-RAM
F-RAM day 3
N-RAM day 3
D
Freezing (%)
Context A
Context C
E
Discrimination index
WT-Vehicle
WT-Retigabine
Nptx1 cKO-Vehicle
Nptx1 cKO-Retigabine
F
G
H
F- or N-RAM-cre
Flex-Nptx2 shRNA
fDIO-hM3Dq-mCherry
PV-flpe mice
I
CNO
J
K
L
Scramble-mCherry
Scramble-hM3Dq
Nptx2 sh-mCherry
Nptx2 sh-hM3Dq
M
N

Figure 5. The effects of activating Kv7.2 or DG PV$^+$ interneurons on memory deficits induced by *Nptxs* depletion in DG engram ensembles. (A, H) Diagram of AAV injection. (B, I) Experimental scheme of memory retrieval test. (C) Representative images of *F*- and *N*-RAM engram cells in DG. Green: *F*-RAM and *N*-RAM ensembles, EYFP, Blue: DAPI. Scale bar: 100 μm. (D, E) The freezing percentage and discrimination index of WT-Vehicle, WT-Retigabine, *Nptx1* cKO-Vehicle and *Nptx1* cKO-Retigabine mice (*F*-RAM). (F, G) The freezing percentage and discrimination index of WT-Vehicle, WT-Retigabine, *Nptx1* cKO-Vehicle and *Nptx1* cKO-Retigabine mice (*N*-RAM). (J) Representative images of *F*- and *N*-RAM engram cells in DG. Green: *F*-RAM and *N*-RAM ensembles, EGFP, Purple: PV$^+$ interneurons, mCherry, Blue: DAPI. Scale bar: 100 μm. (K, L) The freezing percentage and discrimination index of *Scramble*-mCherry, *Scramble*-hM3Dq, *Nptx2 sh*-mCherry and *Nptx2 sh*-hM3Dq groups (*F*-RAM). (M, N) The freezing percentage and discrimination index of *Scramble*-mCherry, *Scramble*-hM3Dq, *Nptx2 sh*-mCherry and *Nptx2 sh*-hM3Dq groups (*N*-RAM). Data are presented as mean ± S.E.M; $^*P < 0.05$, $^{**}P < 0.01$.

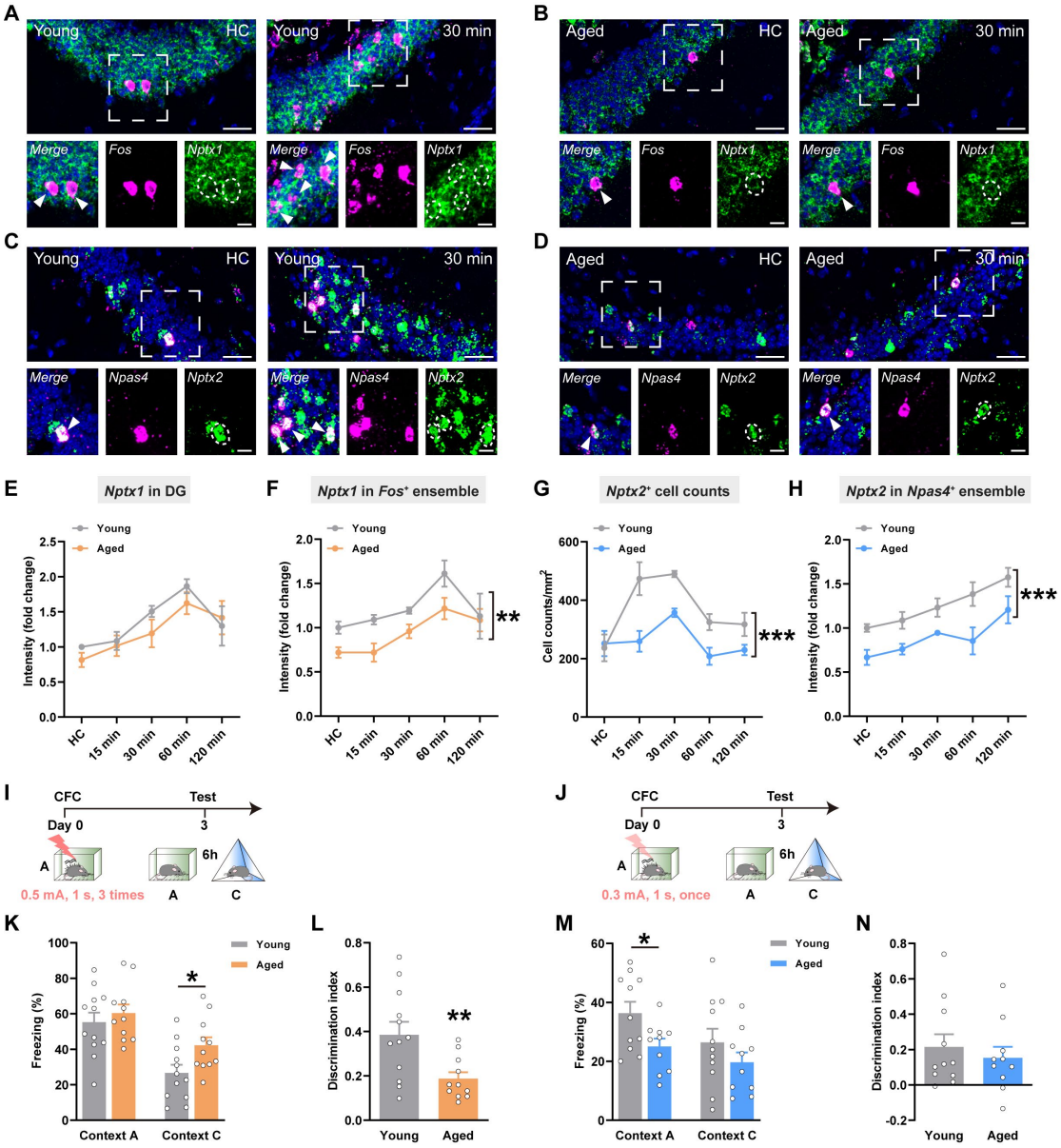

Figure 6. *Nptxs* expression in DG engram cells and contextual fear memory in young and aged mice. (A, B) Representative confocal images of *Nptx1* colocalizing with *Fos* under HC condition and 30 min after CFC in DG of young and aged mice. Green: *Nptx1*, Purple: *Fos*, Blue: DAPI. White arrows indicate the colocalized cells. Scale bar: top, 30 μm, bottom, 10 μm. (C, D) Representative confocal images of *Nptx2* colocalizing with *Npas4* under HC condition and 30 min after CFC in DG of young and aged mice. Green: *Nptx2*, Purple: *Npas4*, Blue: DAPI. White arrows indicate the colocalized cells. Scale bar: top, 30 μm, bottom, 10 μm. (E) The fluorescence intensity

937 of overall *Nptx1* mRNA in DG. (F) The fluorescence intensity of *Nptx1* mRNA in *Fos*$^{+}$

938 ensemble at HC, 15 min, 30 min, 60 min and 120 min after CFC. (G) The *Nptx2*$^{+}$ cell

939 counts in DG. (H) The fluorescence intensity of *Nptx2* mRNA in *Npas4*$^{+}$ ensemble at

940 HC, 15 min, 30 min, 60 min and 120 min after CFC. (I, J) Experimental scheme of CFC

941 to test memory expression. (K, M) The freezing percentages of young and aged mice.

942 (L, N) The discrimination indexes of young and aged mice. Data are presented as mean

943 ± S.E.M; *$P < 0.05$, **$P < 0.01$, ***$P < 0.001$.

944

945

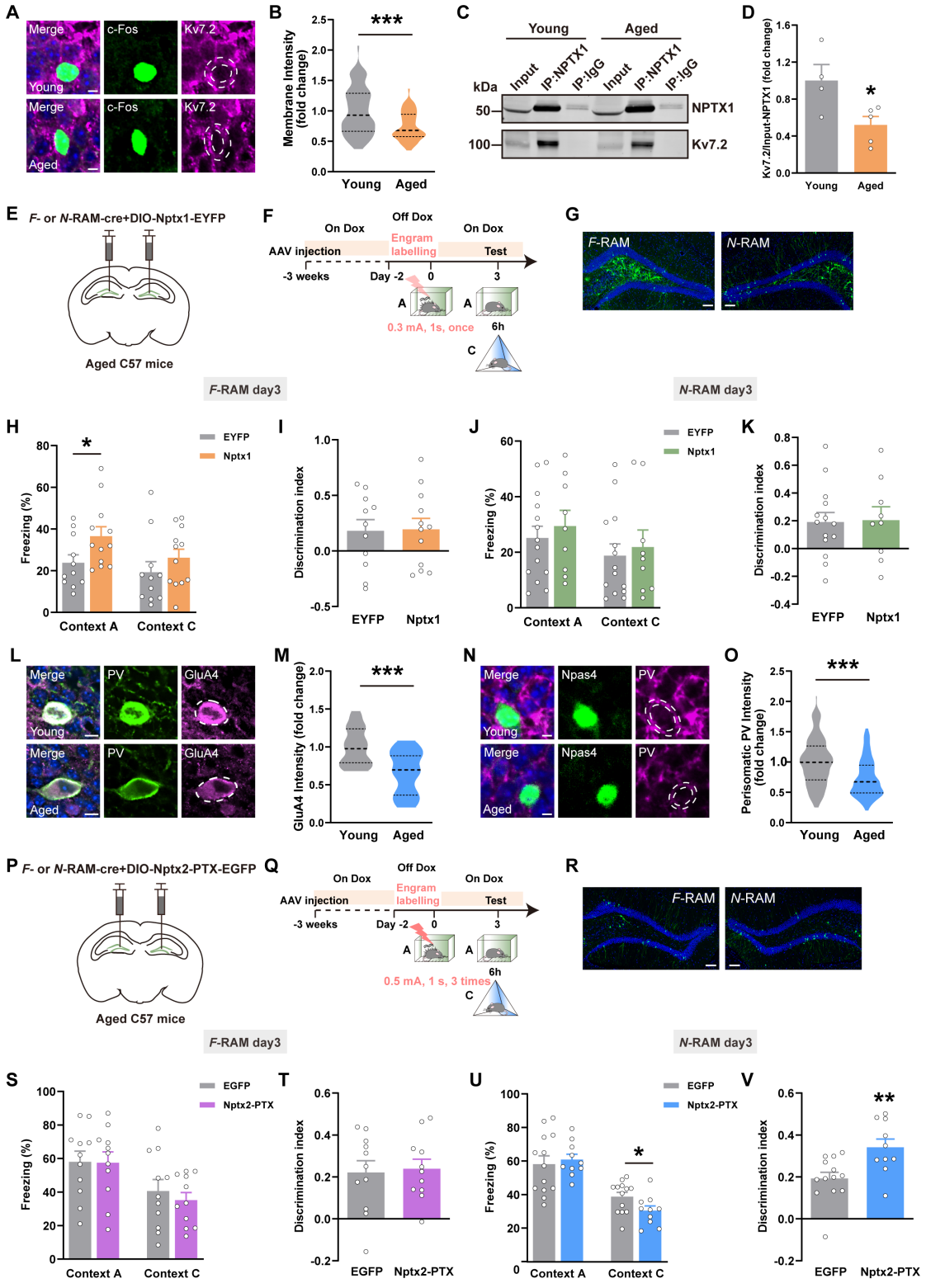
A
Merge
c-Fos
Kv7.2
Young
Aged
B
Membrane Intensity (fold change)
***
Young
Aged
C
Young
Aged
kDa
Input
IP:NPTX1
IP:IgG
50
100
NPTX1
Kv7.2
D
Kv7.2/Input-NPTX1 (fold change)
*
E
F- or N-RAM-cre+DIO-Nptx1-EYFP
Aged C57 mice
F
On Dox
Off Dox
On Dox
AAV injection
Engram labelling
Test
-3 weeks
Day -2
0
3
0.3 mA, 1s, once
6h
G
F-RAM
N-RAM
F-RAM day3
N-RAM day3
H
EYFP
Nptx1
Freezing (%)
Context A
Context C
I
Discrimination index
EYFP
Nptx1
J
Freezing (%)
Context A
Context C
K
Discrimination index
EYFP
Nptx1
L
Merge
PV
GluA4
Young
Aged
M
GluA4 Intensity (fold change)
***
Young
Aged
N
Merge
Npas4
PV
Young
Aged
O
Perisomatic PV Intensity (fold change)
***
Young
Aged
P
F- or N-RAM-cre+DIO-Nptx2-PTX-EGFP
Aged C57 mice
Q
On Dox
Off Dox
On Dox
AAV injection
Engram labelling
Test
-3 weeks
Day -2
0
3
0.5 mA, 1 s, 3 times
6h
R
F-RAM
N-RAM
F-RAM day3
N-RAM day3
S
EGFP
Nptx2-PTX
Freezing (%)
Context A
Context C
T
Discrimination index
EGFP
Nptx2-PTX
U
EGFP
Nptx2-PTX
Freezing (%)
*
Context A
Context C
V
Discrimination index
**
EGFP
Nptx2-PTX

948 **Figure 7. Overexpression of NPTXs in DG engram ensembles rescued memory**
949 **imprecision in aged mice.** (A) Representative confocal images of c-Fos$^+$ cells
950 colocalizing with Kv7.2. Green: c-Fos$^+$ engram cells, Purple: Kv7.2, Blue: DAPI.
951 Dashed white lines outline cell membrane. Scale bar: 5 μm. (B) The average membrane
952 Kv7.2 fluorescence intensity of c-Fos$^+$ neurons in young and aged mice. (C)
953 Immunoblotting of NPTX1 co-immunoprecipitates with Kv7.2 in DG of young and
954 aged mice. (D) The quantification of IP-Kv7.2 in young and aged mice. (E, P) Diagram
955 of AAV injection. (F, Q) Experimental scheme of memory retrieval test. (G, R)
956 Representative expression of NPTX1 or NPTX2-PTX in *F*- or *N*-RAM engram cells in
957 DG. Green: *F*-RAM or *N*-RAM ensemble, EYFP or EGFP, Blue: DAPI. Scale bar: 100
958 μm. (H, I) The freezing percentage and discrimination index of EYFP and Nptx1 aged
959 groups (*F*-RAM). (J, K) The freezing percentage and discrimination index of EYFP and
960 Nptx1 aged groups (*N*-RAM). (L) Representative confocal images of GluA4
961 colocalizing with PV$^+$ interneurons. Green: PV$^+$ interneurons, Purple: GluA4. Scale bar:
962 10 μm. (M) The quantification of GluA4 membrane expression on PV$^+$ interneurons in
963 young and aged mice. (N) Representative confocal images of PV neurites around
964 Npas4$^+$ engram cells. Green: Npas4$^+$ engram cells, Purple: PV, Blue: DAPI. Dashed
965 white lines outline PV neurites. Scale bar: 5 μm. (O) The average fluorescence intensity
966 of PV neurites around Npas4$^+$ neurons in young and aged mice. (S, T) The freezing
967 percentage and discrimination index of EGFP and Nptx2-PTX aged groups (*F*-RAM).
968 (U, V) The freezing percentage and discrimination index of EGFP and Nptx2-PTX aged
969 groups (*N*-RAM). Data are presented as mean ± S.E.M; *$P < 0.05$, **$P < 0.01$, ***$P <$

970 0.001.